



“Preliminary” PhD Thesis

Biocompatible Thin Film Metallic Glasses (TFMGs)

PhD Candidate: Scott Gleason

Supervisor: Professor Michael Ferry

Co-Supervisor: Kevin Laws

ABSTRACT

The aims of this thesis are to produce and examine biodegradable thin film metallic glasses (TFMGs) and the recently discovered ultrastable metallic glass (SMG) films for biomedical applications. To ensure full biocompatibility the films will be composed entirely of essential mineral MgZnCa alloys.

The literature review provides an overview of metallic glass formation and processing, thin films and deposition methods, initial understandings of ultrastable glasses, and biomedical requirements with a focus on biodegradation.

The films will be deposited onto various substrates via magnetron sputtering and pulse laser deposition (PLD) techniques. The master alloys and deposition targets will be prepared via induction furnace melting and copper mould gravity casting of pure base element Mg, Zn, and Ca (99.8wt% pure or better).

The initial results have shown the $\text{Mg}_{65}\text{Zn}_{30}\text{Ca}_5$ alloy is relatively brittle, with most targets fracturing during casting or shaping operations. The targets which were produced without failure were examined via DSC and found to be at best primarily crystalline in structure. This should be expected as this alloy's critical casting thickness is similar to the thickness of the mould utilised.

Going forward XRD analysis will be used to definitively establish the targets' structures, and the target manufacturing process will be refined (current method is not efficient). Numerous thin film metallic glass specimens will be produced via sputtering/PLD and evaluated; hopefully leading to publications and attendance at conferences.

TABLE OF CONTENTS

Abstract.....	i
Table of Contents.....	ii
List of Figures	v
1 Introduction	1
2 Literature Survey.....	2
2.1 Metallic Glasses (MGs).....	2
2.1.1 MGs Properties	2
2.1.2 Theory of MG Production	2
2.1.2.1 Solidification, Super Cooled Liquid (SCL), and Glass Transition (T_g)	2
2.1.2.2 Glass Forming Ability (GFA) and Bulk Metallic Glasses (BMGs).....	3
2.1.2.3 BMG Manufacture Methods.....	4
2.1.2.3.1 Thermoplastic Forming (TPF) Processing.....	5
2.2 Thin Films	6
2.2.1 Thin Film Properties	6
2.2.2 Production via Deposition.....	7
2.2.2.1 Pulsed Laser Deposition (PLD)	7
2.2.2.1.1 PLD Advantages	7
2.2.2.1.2 PLD Challenges.....	7
2.2.2.2 Sputtering Deposition	8
2.2.2.2.1 Direct Current (DC) Sputtering.....	8
2.2.2.2.2 Magnetron Sputtering	9
2.2.2.2.3 Sputtering Advantages.....	9
2.2.2.2.4 Sputtering Challenges	9
2.2.2.3 Preferred PVD Methods.....	10
2.3 Ultrastable Glass (USG).....	10
2.3.1 Ultrastable Metallic Glass (SMG) General Properties, Development, and Production	10
2.3.2 SMG Characterisation and Modelling Techniques.....	11
2.3.2.1 Fictive Temperature (T_f), Kinetic Stability and Enthalpy via Differential Scanning Calorimetry (DSC).....	11
2.3.2.2 The Theoretical Entropy Limit of Glasses and the Kauzmann Temperature (T_k)	12
2.3.2.3 Glass Fragility (m)	13
2.3.2.4 Indentation Modulus (M)	15
2.3.3 SMG Structure, Medium Range Order (MRO)	15
2.3.4 Potential SMG Challenges.....	16

2.3.5	Thin Film Testing Methods	17
2.3.5.1	Adhesion	17
2.4	Biomedical Materials	17
2.4.1	Biomaterial Requirements	17
2.4.1.1	Current Metallic Biomaterials	17
2.4.1.2	Roll of Metallic Elements within the Body	17
2.4.2	Degradation of Biomaterials	18
2.4.2.1	Basic Theory of Corrosion and Its Measurement	18
2.4.2.2	Mg Hydrogen Evolution	19
2.4.2.3	Pitting Corrosion	21
2.4.3	Anti-biotic Scaffolds	22
3	Methods	23
3.1	Target Manufacture	23
3.1.1	Induction Furnace	23
3.1.1.1	Charges Preparation	23
3.1.1.2	Induction Casting of Alloys	23
3.1.2	Shaping of Targets	24
3.2	PVD via Magnetron Sputtering	24
3.2.1	Sputtering of TFMGs and SMGs	24
3.2.2	Sputtering Methods and Initial Parameters	24
3.3	Examined Substrates	25
3.3.1	Water Soluble Substrate	25
3.3.2	BMG Substrate	25
3.3.3	Polycaprolactone (PCL) Scaffolds	25
3.4	Film Characterisation	25
3.4.1	Physical and Chemical Properties	25
3.4.2	Biocompatibility and Bioabsorption	25
3.4.3	Quality of Deposition	25
4	Preliminary Results	26
4.1	Experimental Results	26
4.1.1	Casting Challenges and Observations	26
4.1.2	DSC Scans	26
4.1.3	Target Composition	26
5	References	28
6	Appendices	31
6.1	Glossary	31

LIST OF FIGURES

Figure 1: Schematic of specific enthalpy (h) or specific volume (v) as a function of temperature for a material that exhibits both glass and crystalline solid states. Note 'glass 1' has a greater T_g and accordingly greater h & v than 'glass 2.' This higher temperature stability is the result of 'glass 1' being cooled more quickly than 'glass 2.' Modified from [2].	3
Figure 2: Schematic of critical cooling rate (R_c) and maximum sample thickness (t_{max}) as a function of reduced glass transition temperature (T_g/T_m) for a number of glass forming systems. Note the R_c and t_{max} improve with increasing T_g/T_m . Modified from [6].	4
Figure 3: Schematic TTT diagram where line (1) indicates the slowest cooling rate possible to avoid crystallisation and achieve the metallic glass state, and line (2) an elevated temperature processing window above T_g where metallic glass displays excessive plastic deformation. Reproduced from [7].	6
Figure 4: Schematic of a typical PLD setup showing the incoming laser beam inclined at an approximate 45° angle to the target, and the target and substrate parallel to each other. Modified from [16].	7
Figure 5: Amorphous target XRD scan before (black curve) and after (red curve) PLD showing the shift from characteristic amorphous structure to crystalline. Reproduced from [19].	8
Figure 6: Schematic of a typical DC sputtering setup with an Ar working gas. The high-voltage field generates and propels Ar^+ ions toward the negative target of material "M." Dislodged "M" atoms are hurled in all directions with some being deposited on the positive substrate. Modified from [20].	9
Figure 7: An integrated DSC trace for the molecular IMC glass system displaying the various values of T_f obtained when varying the deposition rate (the coloured line). Note all deposited glasses have a reduced T_f indicating a reduction in enthalpy compared to ordinary glass. Reproduced from [31].	12
Figure 8: Schematic of glass temperature vs entropy in a typical glass forming system. The Kauzmann temperature (T_k) represents the glass transition temperature (T_g) of an ideal glass. The blue line is the extrapolated SCL line and the ideal path. Modified from [31].	13
Figure 9: Viscosity as a function of scaled temperature (T_g/T) for strong to weak glasses over the flowing range of viscosities. Note the 'ideal' strong glass displays a constant exponential slope over the full temperature range, while weaker glass' slopes change. Reproduced from [33].	14
Figure 10: Schematic of the relationship between glass fridity (m) and the enhanced glass transition on glass transition ratio ($\delta T_g/T_g$) for a selection of metallic, molecular, and polymer USGs. Reproduced from [28].	15
Figure 11: Tafel Plot showing the positive anodic Tafle slope β_a , negative cathodic Tafle slope β_c , and their linear extrapolations with their intersection indicating the OCP, and thus the i_{corr} and the E_{corr} positions [44].	19
Figure 12: Plot of hydrogen evolution generated by $Mg_{60+x}Zn_{35-x}Ca_5$ alloys. Note the hydrogen evolution drops off significantly for Zn concentration $>28at\%$. (Filled points are amorphous, open crystalline). Reproduced from [40].	21
Figure 13: Screenshot of the MS Excel tool developed for calculating charge weights, checking alloy composition, and taking notes for improvements in future charges.	23
Figure 14: (a) Crucible for induction furnace melting of alloys, (b) cracked amorphous plate, (c) riser cut free from main casting, and (d) drilled and partly shaped target.	24
Figure 15: DSC trace of the $Mg_{65}Zn_{30}Ca_5$ target plate casting. The trace shows clear endothermic troughs indicating T_m and T_l , but no clear exothermal peaks which would indicate T_g and T_x . This data suggest the casting is primary crystalline.	27

1 INTRODUCTION

Current pharmaceutical technology relies on re-dosing of drugs, often with treatments being readministered several times per day or week. Coating pharmaceuticals with tailored bioabsorbable films designed to degrade over time could allow for a slow controlled release of drug packages such as antibiotics, antimicrobials, and analgesics (painkillers). These medical devices could be implanted during surgeries, eliminating the needs for daily drug administration.

Thin film metallic glasses (TFMGs) are one technology which may make this possible. These novel amorphous metallic materials have been demonstrated to significantly modify substrate properties such as hardness, wear resistance, surface finish, fatigue and corrosion resistance, and even ductility. Recently ultrastable metallic glass (SMG) films have been discovered which display improved thermal and kinetic stabilities, and often reduced entropy relative to the more established TFMGs. Many properties of SMGs have not yet been characterised and it is not yet known if in addition to improved stability if they may offer greater improvements in substrate property modification. The application of these films onto drug delivery systems, or even orthopaedic devices, could provide great potential for improvements in wound healing and pain management practices.

The aims of this thesis are to produce and investigate quality TFMGs and SMGs for biomedical applications. Thin films of established bulk metallic glass (BMG) compositions, such as $\text{Mg}_{65}\text{Zn}_{30}\text{Ca}_5$ will be deposited onto various substrates including; BMGs of similar film composition, Polycaprolactone (PCL) scaffolds, and dissolvable NaCl substrate (to allow base film to be studied independently). The properties and characteristics of the films as well as their property modification effects on the different substrates will be investigated, and the characterised films compared with their BMG counterparts.

2 LITERATURE SURVEY

2.1 METALLIC GLASSES (MGs)

Metallic glasses (MGs) are alloys which exhibit an amorphous structure with no long range order. This lack of an ordered structure results in MGs possess a range of unique properties which make them distinct even from traditional crystalline alloys of similar composition.

2.1.1 MGs Properties

The unique properties of MGs are largely the result of their lack of crystalline structure and grain boundaries, meaning they have essentially eliminated the principal structural and chemical weaknesses in metallic systems. This serves to provide MGs with superior strength, hardness, corrosion, oxidation and wear resistance, reduced thermal and electrical conductivity, and low coefficients of friction when compared with conventional crystalline alloys.

These MG alloys generally also display large amounts of elastic deformation, though their plastic deformation is significantly limited. This results from the amorphous structure's lack of slip systems and dislocation movement; the fundamental mechanism of plastic deformation in crystalline metals. The plastic deformation that is displayed by MGs is via a localised shear band mechanism, but it is very limited. Thus when MGs fail at high stress it tends to be via brittle fracture mechanisms, although it should be emphasised MGs are far less brittle than organic glasses owing to their non-directional metallic bonds [1]. The failure mechanisms of MGs are also highly dependent on temperature and can shift from brittle to ductile, as will be explained later.

2.1.2 Theory of MG Production

The production of MGs requires metallic alloys to be solidified in such a way as to produce stable amorphous structures. This is accomplished via the high cooling rates achieved through rapid quenching from the liquid or vapour states. The physical mechanisms that make this possible are described below.

2.1.2.1 Solidification, Super Cooled Liquid (SCL), and Glass Transition (T_g)

Most liquid materials when cooled to their melting temperature (T_m) undergo a phase change into an ordered solid with a repeating crystalline structure. This is a first-order thermodynamic phase change with the entire process occurring solely at the T_m and being observed as an enthalpy (H) and volume (V) discontinuity. As the ordered structure is at a lower energy and generally more dense than the amorphous liquid both the H and V discontinuities are negative, with a notable exception being water where the V increases.

Despite the thermodynamic driving force liquids are generally cooled below their T_m before they begin to solidify because they require a stable nucleus to initiate the process. This solidification is described by Gibbs Free Energy Theory for homogenous and heterogeneous nucleation. In brief, a stable nuclei initiates solidification by reaching a size where further growth requires less energy than melting, providing the driving force for the phase change. Refer to "Gibbs Free Energy" for specific details not covered here within.

When the liquid is cooled below its T_m without solidifying it is termed a super cooled liquid (SCL). Amorphous solids, or glasses, are formed from SCL by cooling at rates sufficient to suppress the nucleation process entirely. As the SCL is cooled its viscosity (η) increases while its H and V decrease linearly with temperature at the same rate as the liquid state. As the η approaches about $10^{12} \text{ Pa} \cdot \text{s}$ the time scale for molecular rearrangement of the SCL becomes significantly longer than experimental

observation and the SCL is for all practical purposes ‘frozen’ as a glass [2]. This transition occurs at the glass transition temperature (T_g) and is characterised by a decrease in the rate of change of H and V with temperature. Note this is not a phase change, but rather a kinetic event, meaning the material is not technically thermodynamically or kinetically stable, even though it is stable for all intents and purposes [2]. Because of this the actual T_g of a glass depends on the cooling rate (i.e. is not a fixed property like T_m) with faster cooling rates generally resulting in higher T_g , indicating the glass is suitable for use at higher service temperatures, see Figure 1.

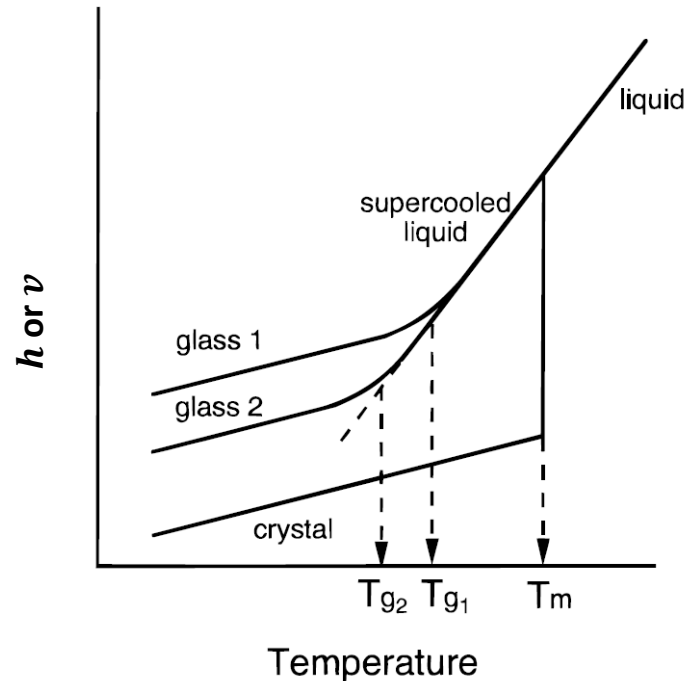


Figure 1: Schematic of specific enthalpy (h) or specific volume (v) as a function of temperature for a material that exhibits both glass and crystalline solid states. Note ‘glass 1’ has a greater T_g and accordingly greater h & v than ‘glass 2.’ This higher temperature stability is the result of ‘glass 1’ being cooled more quickly than ‘glass 2.’ Modified from [2].

2.1.2.2 Glass Forming Ability (GFA) and Bulk Metallic Glasses (BMGs)

The ease at which a material is able to form a glass is termed its glass forming ability (GFA). The GFA is also closely tied to a glass’s stability with high GFAs generally indicating high thermal stability [3]. Organic glasses possess sufficiently high GFAs and thermal stability that the material has been produced since ancient times, and polymers’ GFAs are often high enough they can form glass even with slow cooling rates. In contrast metals have such low GFAs their amorphous glass state was only discovered in 1960 by Klement, et al. [4]. This low GFA results from metals’ high atomic mobility, which allows for MGs’ fast structural relaxation and recrystallization at elevated temperatures [3].

Much of the work on MGs has been to improve their GFAs in order to decrease their critical cooling rate (R_c), the rate of quench required to avoid nucleation into the crystalline state [5]. From these works it has been discovered alloys with their T_g near their T_m have higher GFAs [5, 6]. Meaning the GFA of an alloy increases with its reduced glass transition temperature (T_g/T_m) [5, 6].

From these findings Inoue [5] has formulated three rules for high GFA systems;

1. Multi-component systems of three or more alloy constituents;
2. Significant difference of above 12% in atomic size ratios of the three main constituents; and
3. Negative heats of mixing among the three main constituents (i.e. exothermic reaction).

Alloys that follow these rules display deep eutectics with low T_m , sluggish crystallisation kinetics, and accordingly a high T_g/T_m [5, 7]. The application of these rules has helped to lower R_c sufficiently to allow the produce of three-dimensional amorphous alloys with their smallest dimension being at least 1mm, formally referred to as bulk metallic glass (BMG) formers. These BMGs are superior to MGs as they possess sufficiently high GFAs to allow for these greater dimensions and accordantly display improved thermal stability. As such alloys of BMG composition are of the most interests regardless of a sample's desired dimensions, and all alloy compositions henceforth in these works shall be BMGs unless otherwise noted.

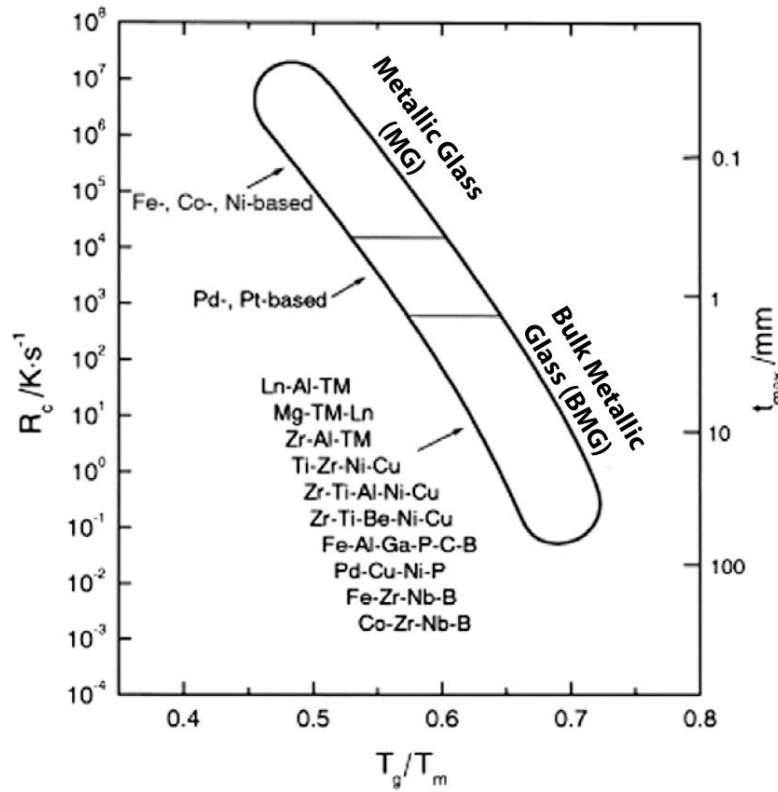


Figure 2: Schematic of critical cooling rate (R_c) and maximum sample thickness (t_{max}) as a function of reduced glass transition temperature (T_g/T_m) for a number of glass forming systems. Note the R_c and t_{max} improve with increasing T_g/T_m . Modified from [6].

The improvements in R_c for amorphous alloy compositions is shown in Figure 2, with the defining moment of BMG development being denoted by the minimum sample thicknesses (t_{max}) reaching the 1mm mark. Note the R_c and t_{max} improve with T_g/T_m signifying alloys' with larger T_g/T_m possess higher GFAs.

2.1.2.3 BMG Manufacture Methods

As mentioned, the production of BMGs requires the alloys be rapidly quenched at a rate equal or better than their R_c in order to avoid crystallisation. For bulk samples these cooling rates are achieved via solidifying the liquid BMG alloys onto copper heat sinks capable of extracting heat at the high rates required. The four standard production methods are:

- Gravity Casting: Molten metal is poured under an air atmosphere into a copper mould to solidify;
- Injection Casting: Molten metal under an inert atmosphere is forced via pressure into a copper mould to solidify;

- Melt Spinning: Molten metal is solidified onto a water cooled copper wheel, producing ribbons of material; and
- Strip Casting: Molten metal is extruded between two water cooled copper rollers, producing continuous plate.

These methods yield cooling rate sufficient for production of simple geometries BMGs, but do not allow for complex shapes. Furthermore secondary processing of BMGs via methods like machining are often impractical do to their brittleness, low thermal conductivity, and the risk of recrystallization via the processing heat additions. However more complex shapes can be accomplished if secondary processing is conducted above BMGs' T_g .

2.1.2.3.1 Thermoplastic Forming (TPF) Processing

A unique property of amorphous metals are once formed they can be heated above their T_g into the SCL temperature range without crystallising for an appreciable amount of time. This is possible because BMGs process sufficient thermal stability above their T_g to maintain their amorphous structure, i.e. the kinetics for crystallisation are slow [7]. At these elevated temperatures BMGs display dramatic softening and superplastically as their η reduces to its SCL values, enabling the constituent atoms to flow more freely past each other.

The introduction of this temporary plastic deformation mechanism allows BMGs to be post-processed via thermoplastic forming (TPF) techniques, similar to thermoplastic polymers. Once the elevated temperature processing is complete the newly formed BMG components can be slowly cooled below their T_g to the glassy state without initiating crystallisation. This slow cooling helps to eliminate internal stresses and allows for high dimensional accuracy in complex BMG components [7]. Note this processing is unique to BMG systems as the more rigid and limited plastic deformation mechanisms of conventional crystalline metallic systems do not support the high deformations of TPF.

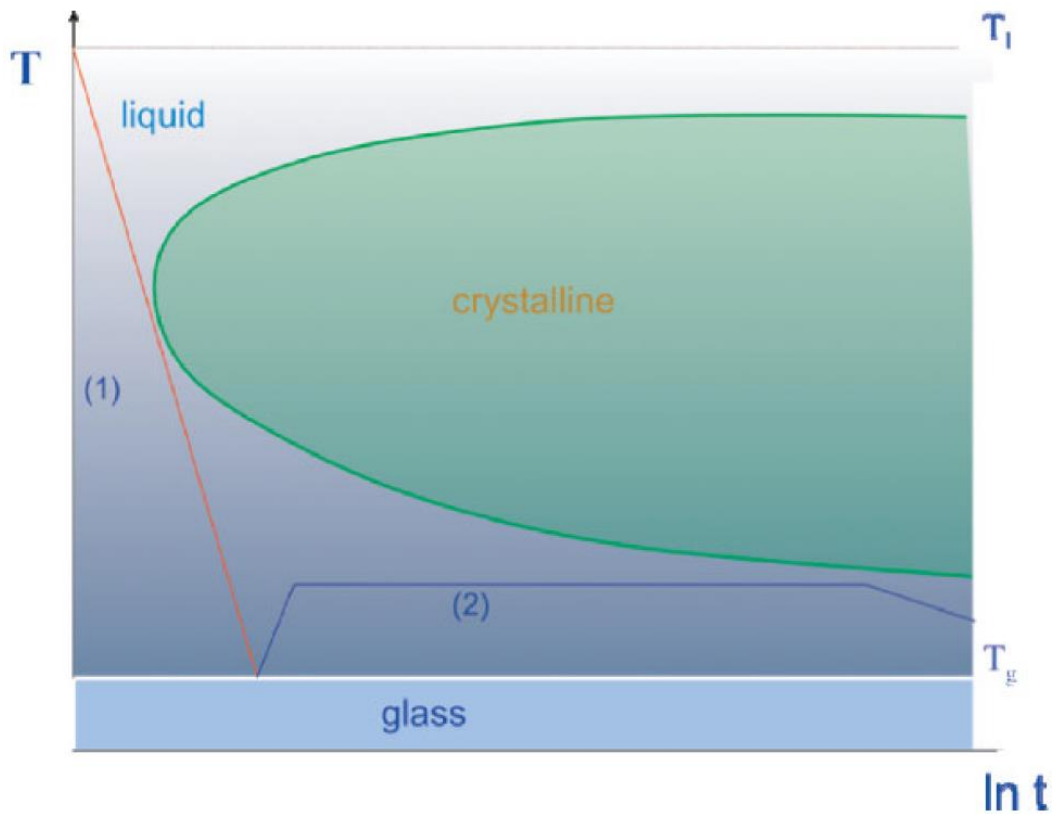


Figure 3: Schematic TTT diagram where line (1) indicates the slowest cooling rate possible to avoid crystallisation and achieve the metallic glass state, and line (2) an elevated temperature processing window above T_g where metallic glass displays excessive plastic deformation. Reproduced from [7].

Figure 3 shows a TTT diagram for a generic BMG. Line (1) of this image shows the minimum R_c quench required to completely avoid crystallisation nucleation when forming the BMG. Line (2) then displays an elevated temperature processing window available for post-processing of the formed BMG. Note with line (2) the processing window stays below the crystallisation zone and displays a gradual cooling once the post processing is complete.

These methods are well suited to the production of BMG substrates, but are unsuitable to forming thin film metallic glass (TFMG). The TFMGs of primary interest for these works must be quenched from the vapour state onto a substrates via deposition techniques.

2.2 THIN FILMS

2.2.1 Thin Film Properties

Thin films are coatings of less than a nanometre to several micrometres in thickness applied to a substrate with the express purpose of modifying the substrate properties. The application of TFMGs to substrates has been shown to have wide spreading effects on properties such as hardness [8], wear residence [9, 10], fatigue properties [11, 12], corrosion residence [13], and surface finish [9, 11, 12, 14]. Chu, et al. [8] has even demonstrated TFMGs can significantly increase BMG substrates' bending ductility via modifying the shear band distribution. This ability to dramatically improving substrate properties, and for the films to often display enhanced properties even from equivalent macro BMGs makes TFMGs an intriguing method for the enhancement of biomaterials.

2.2.2 Production via Deposition

TFMG coatings are readily produced via vapour deposition (VD) processes such as the physical vapour deposition (PVD) processes of pulsed laser deposition (PLD) and sputtering. These processes produce thin films by condensing vaporised material onto a solid substrate under low vacuum.

Note the VD manufacturing route has a significant advantage over traditional BMG liquid casting operations because the composition window is much wider. This is because the rapid quench available from the vapour-to-solid state is much farther from equilibrium than the liquid-to-solid state utilised in BMG casting processes [15].

2.2.2.1 Pulsed Laser Deposition (PLD)

Pulsed laser deposition (PLD) produces films primarily via a thermal process under ultrahigh vacuum (UHV). In the process a 'target' of the desired film material is irradiated and locally vaporised by 45° inclined laser photon pulses. This results in vaporised atoms being ejected from the target as a primarily perpendicular plasma plume, which is directed toward the substrate. Over the course of thousands of repetitions the resulting build-up of atoms produces a thin film (Figure 4).

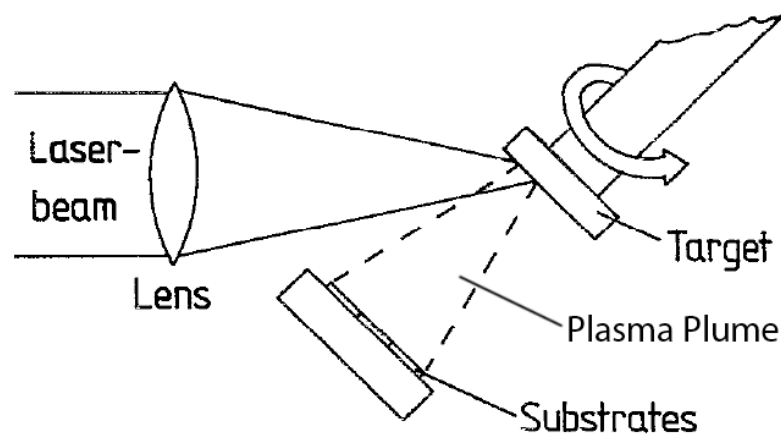


Figure 4: Schematic of a typical PLD setup showing the incoming laser beam inclined at an approximate 45° angle to the target, and the target and substrate parallel to each other. Modified from [16].

2.2.2.1.1 PLD Advantages

The key advantage of PLD is it is able to deposit films of the same stoichiometric ratio, or composition, as its targets [17, 18]. This is significant as it means deposited films have the same elemental composition as their target material. As the compositions of BMGs are generally carefully chosen this is practically useful as it streamlines achieving the desired TFMG compositions.

2.2.2.1.2 PLD Challenges

The work of Cao [19] has identified potential problems in the PLD deposition of TFMGs with achieving quality surface finishes and recrystallization of amorphous targets. It appears the deposition times of the PLD allow for sufficient heat to be applied to amorphous targets to cause partial crystallisation (Figure 5), while still achieving amorphous TFMGs depositions onto the examined crystalline zirconium substrates. As PLD is by definition a thermal deposition process preventing this heat from entering the targets could be difficult. And it remains to be examined if this excess heat could affect the substrates; i.e. recrystallization of amorphous substrates, polycaprolactone (PCL) scaffolds strength, thermal breakdown of the scaffold payloads, etc. Naturally this heat is a moot point when examining standalone TFMGs as these specimens are separated from their substrate after deposition.

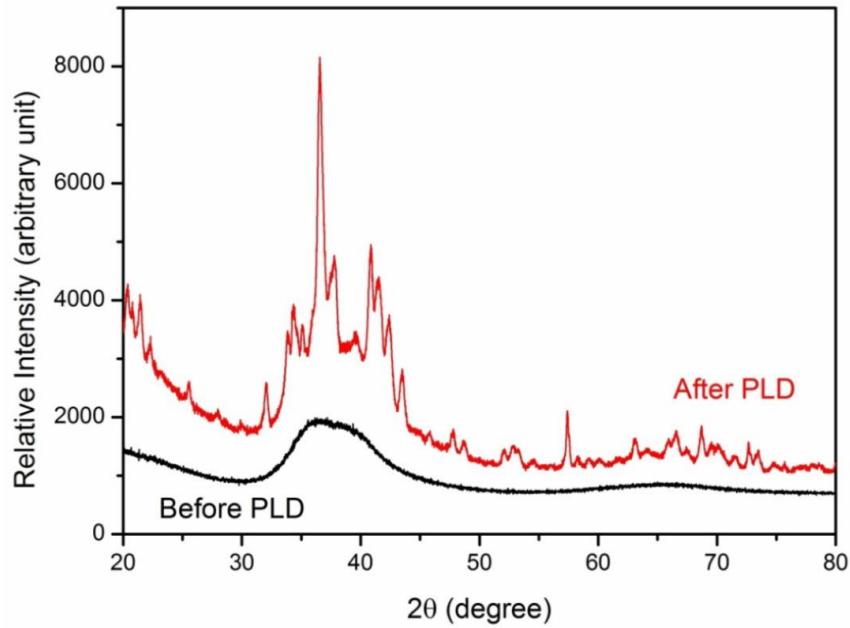


Figure 5: Amorphous target XRD scan before (black curve) and after (red curve) PLD showing the shift from characteristic amorphous structure to crystalline. Reproduced from [19].

PLD TFMG surface finish droplet defects have been observed by Krebs and Bremert [16] and later Cao [19]. It is suggested these defects are intrinsic to the setup configuration and cannot be eliminated by refining the PLD parameters. It is further proposed it may be possible to achieve higher quality surface finishes with setup modifications such as the addition of a mechanical velocity filter to remove slower, droplet depositing prone particles from the plasma plume. Another option is dual-beam ablation geometry which utilised two colliding laser ablation to redirect the coating to a substrate outside the direct path of both plumes, preventing heavier droplet depositing prone particles from reaching the substrate. Notes both of these methodologies reduce the deposition rate and it remains to be seen if these changes are practical to implicate at UNSW.

2.2.2.2 Sputtering Deposition

Sputtering deposition is similar to PLD in that it also coats a substrate with material transferred from a target under vacuum. The essential difference is sputtering utilises the momentum of colliding ions, instead of lasers, to accomplish the transfer.

2.2.2.2.1 Direct Current (DC) Sputtering

Direct Current (DC) sputtering applies a high-voltage to create a circuit between the target and substrate, forming a negative (cathode) and positive (anode) electrode respectively. The high-voltage field generated within the chamber ionises the low pressure inert working gas, generally Argon, causing the now positive ions to be attracted to the negative target. The charged ions collide with the target and dislodge atoms as a plasma from its surface, which are expelled in all directions. A portion of these free atoms come in contact with the substrate surface and are deposited as the coating (Figure 6).

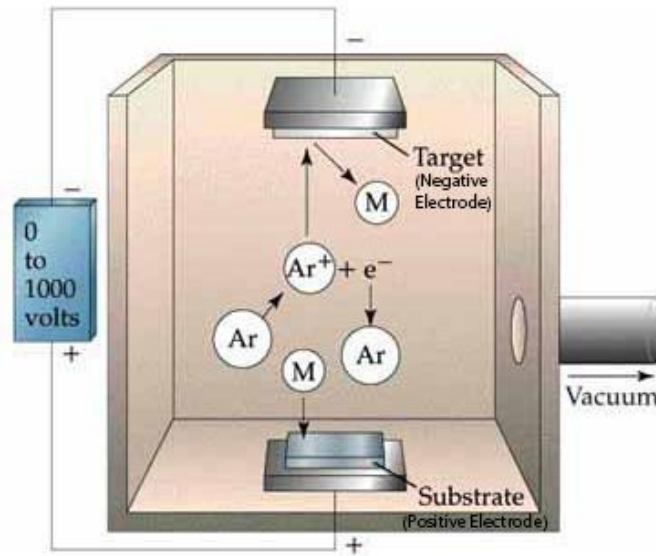


Figure 6: Schematic of a typical DC sputtering setup with an Ar working gas. The high-voltage field generates and propels Ar^+ ions toward the negative target of material "M." Dislodged "M" atoms are hurled in all directions with some being deposited on the positive substrate. Modified from [20].

The key advantage of DC sputtering when working with amorphous materials is it able to accommodate low working temperatures as the mechanical mechanism avoids adding unnecessary heat to targets and substrates. Additionally, while Ar is a convenient working gas, greater deposition efficiency can be achieved when coating with lighter or heavier elements by working with lighter or heavier inert gases, respectively. These characteristics help make it possible to deposit most BMGs via DC sputtering.

2.2.2.2.2 Magnetron Sputtering

Magnetron sputtering is a variant of DC sputtering which improves ionisation efficiency by applying a magnetic field to trap the charged Ar^+ ions near the target surface. This variant is prevalent in most recent studies and all further mention of sputtering shall be magnetron sputtering, unless otherwise noted.

2.2.2.2.3 Sputtering Advantages

While the momentum exchange mechanism of sputtering allows for the use of amorphous targets when depositing TFMG (i.e. excess heat is not added to the system) it has been found the use of crystalline targets results in no appreciable difference in the quality, composition, and structure of the substrate coating [21]. Instead, as shown by Liu, et al. [21] work on the $\text{Zr}_{55}\text{Cu}_{30}\text{Ni}_5\text{Al}_{10}$ system, the coating quality and production of TFMG is primarily controlled by the Ar pressure and sputtering power parameters. This has implications for practical application production runs as crystalline targets are easier, quicker and cheaper to produce than amorphous ones.

When depositing TFMGs it has been observed the deposition rate is proportional to the sputtering power, and that higher rates result in smoother film surfaces [19, 21]. Additionally, Liu, et al. [21] have found a dynamic smoothing effect occurs making it possible to produce atomically flat TFMGs with low Ar pressure and high sputtering power.

2.2.2.2.4 Sputtering Challenges

One of the core challenges with single target magnetron sputtering is it can be difficult to achieve the same stoichiometric ratio (i.e. composition) as the target alloy when depositing multi-component TFMGs [19, 21, 22]. This can occur because of the different sputtering yields of composition target

elements when subjected to ion bombardment. It is possible to remedy the situation through the use of multiple pure element targets, called combination deposition [23-25], but as shown by Liu, et al. [21] this method may not be necessary. Liu, et al. [21] found it is possible to deposit TFMGs with the same composition as their $\text{Zr}_{55}\text{Cu}_{30}\text{Ni}_5\text{Al}_{10}$ target by refining the Ar pressure and sputtering power parameters. As this solution requires only a single target and no modifications to the sputtering set up it seems reasonable to examine it first with the Mg based systems.

2.2.2.3 Preferred PVD Methods

Thus despite sputtering having more difficulties than PLD when refining the stoichiometric ratios for deposition, it has been concluded it the superior deposition method. This is primarily because of its significant advantages; non-thermal process, higher operating pressures, faster deposition rates, and better surface finishes. For these reason sputtering shall be the preferred method for TFMG deposition in these works.

2.3 ULTRASTABLE GLASS (USG)

Ultrastable glasses (USGs) are amorphous films in a low energy state produced via VD techniques and generally characterised by their high thermodynamic and kinetic stabilities, low entropy, high density, high elastic modulus, and always by an enhanced glass transition temperature (δT_g). The δT_g phenomenon is their defining characteristic as it indicates the high kinetic stability due to the higher temperatures required to dislodge their atoms from the glassy configuration [26, 27]. This naturally extends to give USGs higher service temperatures, and hence higher softening temperatures relative to their ordinary glass counterparts.

2.3.1 Ultrastable Metallic Glass (SMG) General Properties, Development, and Production

The defining characteristic of USGs are the δT_g and accordingly their high kinetic stability. They also generally are at a low-thermodynamic-energy state exhibited by low enthalpy, have a high density, and possess a high elastic modulus. These effects can be significant as demonstrated by Aji, et al. [3] whom produced materials with 30% gains in elastic modulus and hardness.

To date the only developed USGs are organic, molecular and polymer glasses, with only a handful of attempts being made to produce ultrastable metallic glasses (SMGs) [3, 28, 29]. Part of the reason for this is it unclear if the more simple atomic structures of metallic alloys, relatively to molecular and polymer glasses, are suitable to form USGs [28]. Nevertheless the work of Yu, et al. [28], Aji, et al. [3], and Wang, et al. [29] on Zr and Au alloy systems have established the initial understandings of what appear to be SMGs, though it remains to be seen how the established trends will extend to other metallic systems.

Production of USGs is via low rate, low pressure VD techniques onto substrates at elevated temperature [3, 28, 29]. This method allows sufficient time for the molecular relaxation kinetics of glasses to rearrange into highly efficient packing structures [3, 26, 29]. With the initial work on USGs showing the more complicated the deposition material's atomic structure the higher the substrate temperature (T_{sub}) must be [28]. Accordingly the ideal T_{sub} for a SMG is $0.7 - 0.8 T_g$, while it is $0.75 - 0.85 T_g$ for the more complicated molecular glasses [26-28, 30, 31]. Yu, et al. [28] has gone on to note that while more complicated atomic structures require higher temperatures to arrange into USG configurations no definite mechanism has been identified for why the ideal ranges are well below the USGs' T_g . Theoretically higher temperatures should allow for more efficient rearrangement of atoms, but this does not happen as it appears there are an unidentified limiting factors. However it is

anticipated the simple atomic structure of SMGs could serve as model material in the study of glass thermodynamics and kinetics phenomena [28, 29].

Non-VD production techniques do not allow sufficient rearrangement time to form USGs as is demonstrated by organic glass where a reduction in cooling rate by a factor of 10 typically only decreases the T_g by 3 – 5 kelvin [2, 27]. The results of the VD techniques cannot even be replicated with extensive artificial aging or annealing times below T_g . For example Swallen, et al. [26] found with molecular glass the ultrastable effects could not be replicated even when annealed below their T_g for 6 months, and when working with Kearns, et al. [31] went on to show the theoretical annealing time required would be at least 1000 years. Additionally both Aji, et al. [3] and Wang, et al. [29] showed annealing SMGs can completely remove the ultrastable effects, implying any production materials should have their service temperatures and thermal creep carefully evaluated.

2.3.2 SMG Characterisation and Modelling Techniques

Additional insight into the thermodynamic and kinetic stability, general properties, and structure of SMGs have been identified via a number of characterisation and modelling techniques.

2.3.2.1 Fictive Temperature (T_f), Kinetic Stability and Enthalpy via Differential Scanning Calorimetry (DSC)

Differential scanning calorimetry (DSC) is an analytical technique that measures the heat flow of an unknown sample. This is done by raising its temperature linearly at the same rate as a reference sample with a known heat capacity. This allows phase changes to be detected in the unknown sample as more or less heat will need to be applied to it to maintain both samples at the same temperature. This can be used to detect melting, crystallising, and more subtle changes like glass transition in a sample.

With amorphous materials the analysis displays an exothermic ‘step in the baseline’ as the sample reaches its T_g because it undergoes a change in its heat capacity. Upon further heating many amorphous materials spontaneously rearrange themselves into an ordered crystalline structure. This Crystallisation temperature (T_x) is recorded as an exothermic peak. With further heating the melting temperature (T_m) and liquidus temperature (T_l) are reached and recorded as endothermic peaks, absorbing energy.

Using DSC the kinetic stability of glass can be measured by shifts in the onset temperature (T_{onset}), which appear as the first ‘step in the baseline’ in the DSC specific heat capacity (C_p) trace; identifying the start of the T_g region. Shifts in the T_{onset} to higher temperatures identify an increase in heat capacity as the atoms need to absorb more energy to become mobile; indicating the higher kinetic stability with a higher T_g [31]. The value of the T_g is generally taken as the maxima of the derivative of trace with respect to temperature.

A specific enthalpy (h) curve from the DSC trace can be obtained by integrating the original C_p trace, with respect to temperature. Using this curve the fictive temperature (T_f) can be used to establish the enthalpy of the glass by measuring where the film’s enthalpy line intersects the extrapolated SCL enthalpy line of the bulk material (Figure 7) [31]. An ordinary glass’s enthalpy appears at $T_f = T_g$ on the trace, whereas an ultrastable glass’s is expected to have a lower T_f and lower enthalpy at $T_f < T_g$.

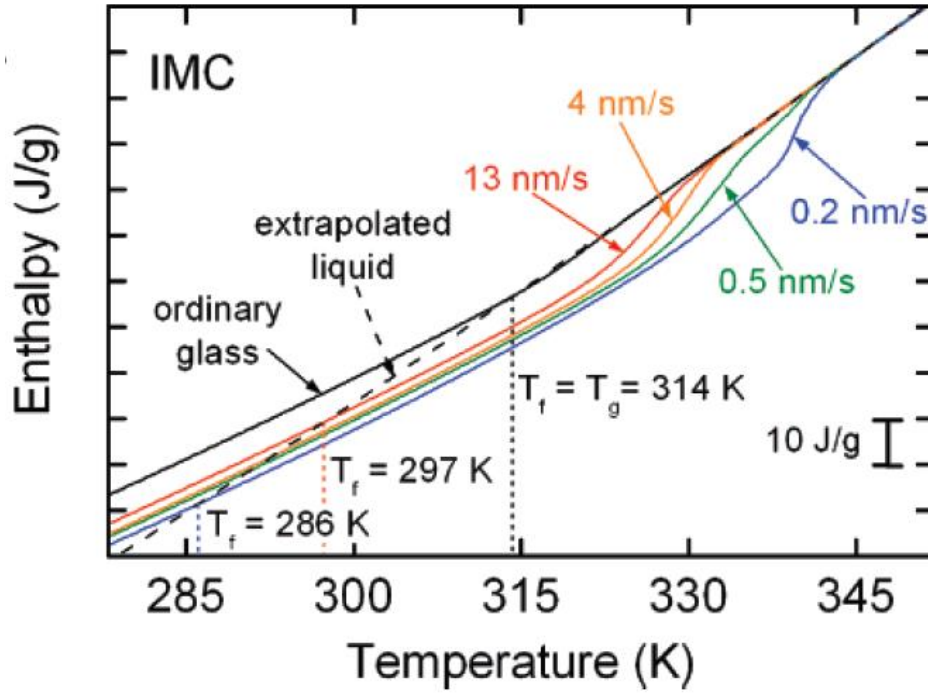


Figure 7: An integrated DSC trace for the molecular IMC glass system displaying the various values of T_f obtained when varying the deposition rate (the coloured line). Note all deposited glasses have a reduced T_f indicating a reduction in enthalpy compared to ordinary glass. Reproduced from [31].

Most developed USGs and the new SMGs display reduced enthalpy, as improved stability predicts [3, 29]. However the work Yu, et al. [28] and Guo, et al. [32] on SMGs and polymer USGs respectively have shown exceptions with high enthalpy being coupled with high kinetic stability δT_g . When this occurs the enthalpy traces of USGs are greater than ordinary glass and intersect higher on the SCL line with $T_f > T_g$. This contradiction with Kearns, et al. [31] demonstrates that T_{onset} and T_f are not coupled together and act independently in USG systems. Accordingly both parameters should be examined when studying new SMG materials.

2.3.2.2 The Theoretical Entropy Limit of Glasses and the Kauzmann Temperature (T_k)

Normally a glass is formed when a material's SCL solidifies on reaching its T_g . However if the SCL could be lowered to the entropy (S) of its crystalline state it would achieve the theoretical lowest thermodynamic-energy state possible and its 'ideal' T_g , known as the Kauzmann temperature (T_k), (Figure 8) [26, 31]. This makes T_k a useful limit to evaluate the effectiveness of the improvements in thermodynamic stability of USGs.

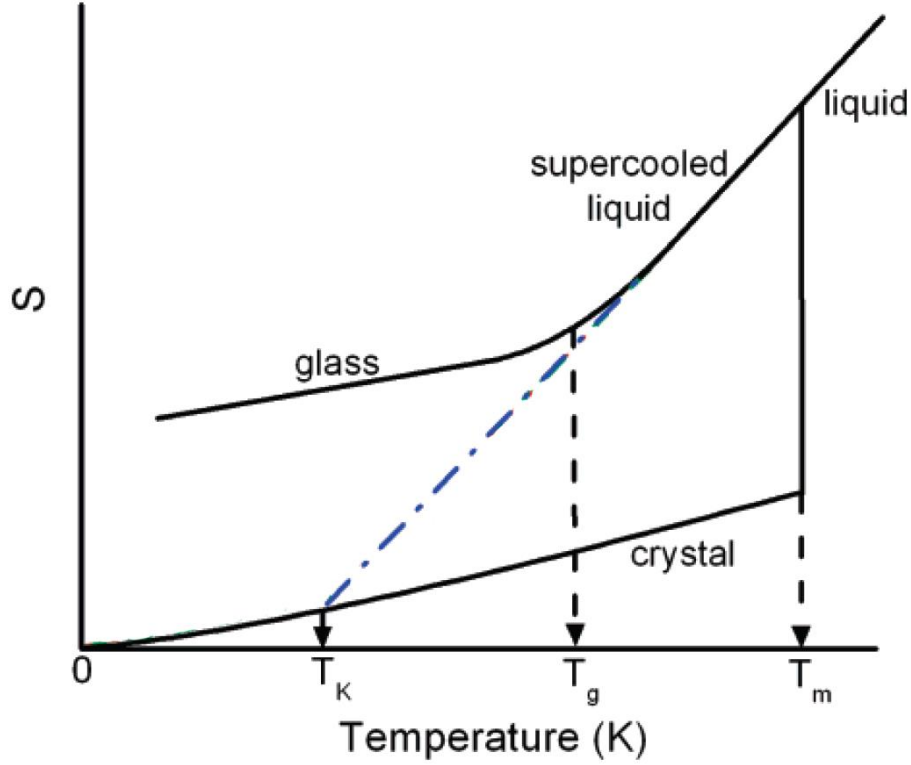


Figure 8: Schematic of glass temperature vs entropy in a typical glass forming system. The Kauzmann temperature (T_K) represents the glass transition temperature (T_g) of an ideal glass. The blue line is the extrapolated SCL line and the ideal path. Modified from [31].

Rewriting Swallen, et al. [26] and Kearns, et al. [31] equation for proportion along the energy landscape (θ_k) to measure between T_K and T_g the following expression is obtained.

$$\theta_k = 1 - \frac{T_g - T_f}{T_g - T_K} \quad (2.1)$$

Equation (2.1) follows the extrapolation SCL line of a glass and calculates an entropy ratio relative to the glass's ideal T_K and its T_g . From this it is seen an ideal glass with $T_f = T_K$ results in $\theta_k = 0.0$, signifying the glass has reached the bottom of the energy landscape [26, 31]. While an ordinary glass with $T_f = T_g$ results in $\theta_k = 1.0$, signifying the glass has not moved down the energy landscape (it is 100% the distance between T_K and T_g).

Thus for real USGs with reduced entropy the θ_k falls between 0.0 and 1.0, while the higher entropy SMGs of Yu, et al. [28] would yield θ_k greater than 1.0, indicating they have moving up the energy landscape past the T_g datum. For example, a $\theta_k = 1.25$ would indicate a glass's entropy is 125% greater than its ideal T_K glass.

2.3.2.3 Glass Fragility (m)

The fragility (m) of a glass is a measure of its deviation from ideal Arrhenius behaviour; defined as the rate of change of the glass's viscosity (η) as a function of inverse temperature (T), scaled to the glass's T_g .

$$m \equiv \left. \frac{\partial \log_{10}(\eta)}{\partial \left(\frac{T_g}{T}\right)} \right|_{T=T_g} \quad (2.2)$$

The more a glass varies from this ideal Arrhenius behaviour the more ‘fragile’ it is, and higher its m value. Highly fragile glasses, or ‘weak’ glasses, vary significantly from the ideal Arrhenius behaviour, and generally experience substantial deviations in heat capacity with temperature [33]. In contrast low fragility, or ‘strong’ glasses, have little variation from Arrhenius behaviour and usually experience little change in heat capacity with temperature. Whether a glass is strong or weak typically depends on the atomic structure, with BMGs generally characterised as ‘strong’, polymers as ‘weak,’ and molecular glasses somewhere in between, see Figure 9.

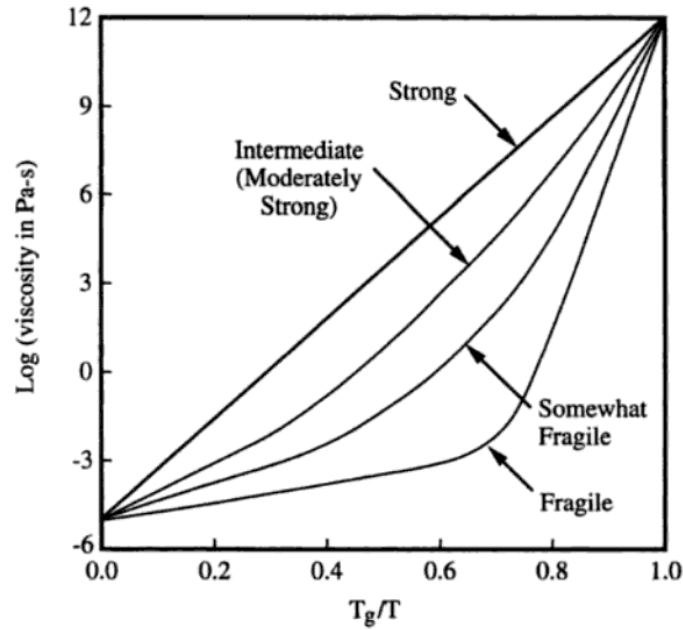


Figure 9: Viscosity as a function of scaled temperature (T_g/T) for strong to weak glasses over the flowing range of viscosities. Note the ‘ideal’ strong glass displays a constant exponential slope over the full temperature range, while weaker glass’ slopes change. Reproduced from [33].

Yu, et al. [28] found m of metallic, molecular, and polymer USGs correlate with $\delta T_g/T_g$, which is surprising given the notable difference in their atomic structures, bonding, and deposition rates (Figure 10). From these initial findings it appears greater improvements in δT_g in relation to the standard T_g correlates with more fragile glasses (i.e. high m values supports high δT_g). Although the SMGs of Yu, et al. [28] were the only metallic glasses used in this analysis, this initial data would suggest the δT_g improvements for SMGs may have a modest limit.

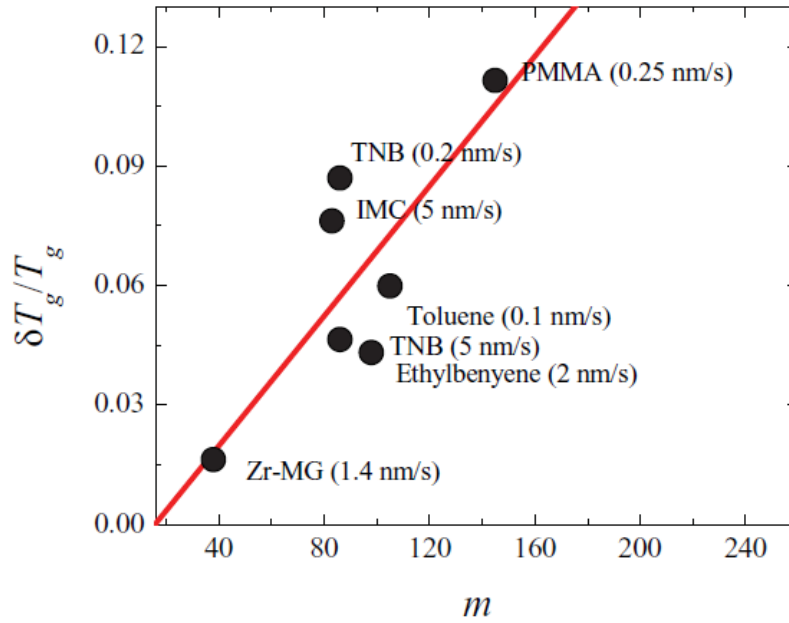


Figure 10: Schematic of the relationship between glass fridity (m) and the enhanced glass transition on glass transition ratio ($\delta T_g/T_g$) for a selection of metallic, molecular, and polymer USGs. Reproduced from [28].

2.3.2.4 Indentation Modulus (M)

The indentation modulus (M) of a material is an elastic constant which accounts for compressive and shear deformations with compressive load. It is given by;

$$M \equiv \frac{E}{(1 - \nu^2)} \quad (2.3)$$

The initial work of Yu, et al. [28] has found a modest increase in M for SMGs over BMGs of 5 – 10 % for the ultrastable $\text{Zr}_{65}\text{Cu}_{27.5}\text{Al}_{7.5}$ system, indicating SMG may be able to better support compressive loads.

2.3.3 SMG Structure, Medium Range Order (MRO)

From molecular glasses it is expected USGs will be distinguishable from normal glasses by extra-low angle peaks in XRD analysis. However Yu, et al. [28] have observed this is not the case with SMGs as the analysis appears identical to BMGs, implying SMGs' corresponding states of packing are not significantly different. This difficulty was also encountered by Aji, et al. [3] whom were also unable to differentiation between ordinary and ultrastable glass via XRD and HRTEM. However Yu, et al. [28] went on to suggest there may be a hidden polyamorphous or layer-like super-structures in the SMGs, although they were unable to confirm it.

Using STEM techniques Aji, et al. [3] were able to identify medium range order (MRO) structures of 2nm in their $\text{Zr}_{55}\text{Cu}_{30}\text{Ni}_5\text{Al}_{10}$ SMG, which they believe are responsible for the ultrastable effects. Via Angstrom beam electron diffraction (ABED) Aji, et al. [3] examined the MRO further and found it is not composed of any of the alloy's known simple crystal structures, but are instead distorted icosahedra with local crystal-like cube symmetry. Aji, et al. [3] believe this MRO is responsible for the SMG stability characteristics and offers explanation for why only VD techniques can produce SMG. The MRO occurs when tens to hundreds of atoms are arranged in the energy minima, but do not form in ordinary glass because solidification from liquid, or annealing already formed glass at elevated temperature, does

not allow sufficient time for MRO formation. Conversely the slow VD techniques used in forming USGs allows the surface atoms to arrange themselves into the highly order MRO structures before being covered by later arriving atoms, similar to layered 3D-printing.

2.3.4 Potential SMG Challenges

Investigation has identified potential issues and challenges with the demonstrated PVD pressures and T_{sub} required when producing SMGs. For example, Qin, et al. [24] has found in the binary amorphous $Zr_{65}Cu_{35}$ system raising substrates to just room temperature can cause crystallisation of films if the Ar pressure is not properly refined. This appears concerning as the alloy constituents of this system are in comparable amounts with the Yu, et al. [28] and Aji, et al. [3] systems of $Zr_{65}Cu_{27.5}Al_{7.5}$ and $Zr_{55}Cu_{30}Ni_5Al_{10}$ respectively. Additionally Aji, et al. [3] found more simple binary and ternary system SMGs were more difficult to produce, had more modest gains in T_g and T_x , and often contained crystalline phases. However these findings support the theory simple atomic structure metallic alloys may not be suitable to form SMGs, and it may be only more atomically complicated BMGs, such as high GFA ternary systems, are suitable to form SMGs [28]. As this research will be working with ternary Mg systems, it is believed they will be sufficiently atomically complicated to form SMGs.

It is known from Liu, et al. [21] and Cao [19] that higher deposition rates result in smoother TFMGs, while Kearns, et al. [31] work with molecular USGs has found lower deposition rates produce more kinetically stable, lower enthalpy glasses. The effects of deposition rate on SMG production were not examined by Yu, et al. [28], Aji, et al. [3], and Wang, et al. [29], but there was a significant difference in deposition rate used by the three groups. Both Aji, et al. [3], and Wang, et al. [29] made use of very slow deposition rates of less than 0.2nm/s to produced their SMGs with both materials displacing the ideal behaviour of high kinetic stability coupled with low enthalpy. However Yu, et al. [28] made use of deposited rate almost a magnitude higher, 1.4nm/s and produced an SMGs possessing both high kinetic stability and high enthalpy. As Yu, et al. [28] and Aji, et al. [3] had similar SMGs of $Zr_{65}Cu_{27.5}Al_{7.5}$ and $Zr_{55}Cu_{30}Ni_5Al_{10}$ respectively, these observations would suggest it may be possible to produce lower enthalpy SMGs by lowing the deposition rates, although if the TFMG trends hold the films may become more rough. These effects should be examined in new research as there is no body of work on varying SMG deposition rate and the reliability of TFMG trends has not been confirmed to translate to SMG systems.

Interestingly Schlüter, et al. [34] have already examined the MgZnCa system ($Mg_{45}Zn_{50}Ca_5$ and $Mg_{60}Zn_{35}Ca_5$) over various power and deposition rates to produce thin films. They found high power/deposition rates result in crystalline films while lower rates are able to deposit fully amorphous TFMG [34]. They came to the conclusion the higher powers allow sufficient heat to be added to the substrate for crystallisation to occur [34]. Wang, et al. [29] found similar results working with $Au_{52}Ag_5Pd_2Cu_{25}Si_{10}Al_6$ SMG where they showed the heat additions of the magnetron sputtering plasma can be attributed to a 20K temperature fluctuation at the substrate. This alloy has a fairly low T_g of 400K meanings its ideal T_{sub} for SMG deposition is around room temperature, making these 5% of T_g fluctuations significant. Additionally MgZnCa based bio-alloys have a similar low T_g (405K for $Mg_{65}Zn_{30}Ca_5$) suggesting their substrates can be expected to experience the same 20K temperature fluctuation.

These findings raise important question as to how high deposition power can be in the Mg system without the risk of elevated T_{sub} exceeding the ideal range and resulting in TFMG or crystalline films instead SMG films. Can SMG deposition power parameters be refined to the point that no substrate heat addition is needed to produce ultrastable materials, or that substrates will needed to be cooled?

These are significant as the implications suggest a possibility of reduced production cost through higher production rates, and reduced energy use.

2.3.5 Thin Film Testing Methods

2.3.5.1 Adhesion

Scratch tests can be used to ascertain the film adhesion.

The adhesion of films is readily tested via scat methods [35-38].

2.4 BIOMEDICAL MATERIALS

Biomaterials are materials designed for use within a human or other animal's body for a medical purpose. This task requires the materials to be biocompatible, which is taken to mean they must not adversely affect the body. Generally this requirement has been met via the use of bio-inert materials like Ti or certain polymers which do not interact with the body and do not significantly degrade or corrode. After these bio-inert materials have served their function, they often have to be removed via secondary surgeries.

2.4.1 Biomaterial Requirements

In vivo biomaterials are medical devices designed to aid in healing via performing part of the body's internal functions. They are approved and tested by regulatory organisations like the Food and Drug Administration (FDA) in the USA, and the Therapeutic Goods Administration (TGA) in Australia. To gain approval devices are subjected to a series of biocompatibility tests which establish the body's acceptance to them in the surrounding tissues and the body as a whole. Actual passing requirements are dependent on the consequence of failure (i.e. heart valves have stringent requirements as failure can result in death), but as minimal requirements, *in vivo* medical device treatment should not result in any of the following:

- Irritate the surrounding structures;
- Provoke an abnormal inflammatory response;
- Incite allergic or immunologic reactions; or
- Cause cancer.

2.4.1.1 Current Metallic Biomaterials

Traditional metallic biomaterials like stainless steels and Ti are designed to be bio-inert and not degrade within the body. After severing their function they must be removed via secondary surgeries unless they have been designed to remain in the body permanently. There is also a significant mismatch between their high stiffness and strength relative to bone, which in orthopaedic applications can result in stress shielding.

Stress shielding is a reduction in bone density and strength which results from reduced stimulus during bone remodelling. It occurs around orthopaedic implants because they are able to carry significant loads and thus the bones are not thoroughly stimulated. Mg implants are less sustainable to this phenomena because their elastic modulus (E) is only about 41 – 45 GPa, which is much closer to human bone's 3 – 20 GPa than other metallic biomaterials [39, 40].

2.4.1.2 Roll of Metallic Elements within the Body

Essential bio-absorbable metallic elements are critical for proper bodily function and when metabolised can aid in the healing process. This makes the elements of Mg, Zn, and Ca ideal major alloy constituents for biodegradable alloys. Moreover, as these elements are water soluble any reasonable excess can be safely excreted from the body via urination.

Mg plays a critical role in numerous reactions within the body. It is an activator in many enzyme reactions, co-regulator in protein synthesis and muscle contraction, and stabiliser of RNA and DNA [41]. In the past, when used as an *in vivo* biomaterial Mg has also been linked to stimulating new bone growth [42]. Zn is a trace element in the body which appears in enzyme classes and in muscles [41]. Ca is well known for its structure function in the skeleton, but also has a signal function in muscle contractions, blood clotting, and cell function [41]. Other essential minerals which can be safely used in bio-absorbable alloys include Fe and Mn.

Other elements like Al and rare earths (RE) have also been alloyed with Mg in past, but their use is not ideal as they are known to not meet the necessary biomaterial requirements. For example, Al has been linked to neurological disorders such as Alzheimers disease [41]. Even though the body can tolerate toxic elements in small quantities it is not ideal, and they will not be considered for bio-corrosion applications in these works.

2.4.2 Degradation of Biomaterials

Ideally essential metallic element biodegradable alloys are designed to undergo controlled corrosion *in vivo* throughout the tissue healing process. This gradually releases corrosion products around the injury site throughout the healing process, which are either metabolised to assist with the healing or simply excreted. Once healing is complete the support of the biodegradable alloys is no longer needed. They continue to degrade ultimately corroding completely to leave no implant residues, and eliminating the need for secondary removal surgeries.

2.4.2.1 Basic Theory of Corrosion and Its Measurement

Corrosion is an electrochemical reaction describing the flow of electrons which occurs when a physical electrical connection exist between an anode and a cathode via an electrolyte medium. By convention, electrons will flow from the negative anode to the positive cathode, resulting in oxidation at the anode and reduction at the cathode.

The kinetics of the corrosion reaction acting upon a specimen can be measured via potentiodynamic polarisation (PDP) scans, in which the rate of the anodic or cathodic reactions on the specimen (i.e. the working electrode) are represented by the current density (i.e. current per unit area). The rate of the corrosion reaction can be significantly affected by numerous variables including temperature, specimen surface condition [43], and the chemical environment and thus these should be carefully controlled and standardised.

The polarisation scans are performed via controlling the anodic or cathodic reactions' driving force, AKA their potential (V), and observing the applied current density required to produce the desired variations in potential. The anodic scans start at low potentials and ramp up, whereas the cathodic start at high potentials and ramp down, hence by convention anodic currents are positive and cathodic negative. The slowest corrosion rate will occur when the anodic and cathodic currents equal each other and the applied current density is at its minimum (theoretically zero); this is known as the open circuit potential (OCP).

The Tafel equation (Equation (2.4)) and Tafel Plots are tools used to interpret the data generated by PDP scans. The Tafel equation expresses the anodic or cathodic reactions' current density as a function of their overpotential (η); overpotential being defined as the difference between the applied potential (E_A) and OCP (E_{OCP}).

$$\eta = E_A - E_{OCP} = \beta \log \frac{i}{i_0} \quad (2.4)$$

Where β is the Tafel slope, i the applied current density, and i_0 the exchange current density.

Plotting the Tafel equation for both the anodic and cathodic reactions produces the Tafel Plot (Figure 11) for the corrosion reaction. From the plot the OCP, where anodic and cathodic currents are equal, can be obtained via extrapolation. This is performed along the linear region of the anodic and cathodic β slopes, with the extrapolations' intersection indicating the OCP. The current density and potential coordinates of the OCP on the plot indicate the corrosion current density (i_{corr}), and corrosion potential (E_{corr}) for the reaction. When evaluating improved corrosion resistance the idea specimen will have both a more noble potential (i.e. E_{corr} is greater), and a reduced i_{corr} in relation to the comparison specimen.

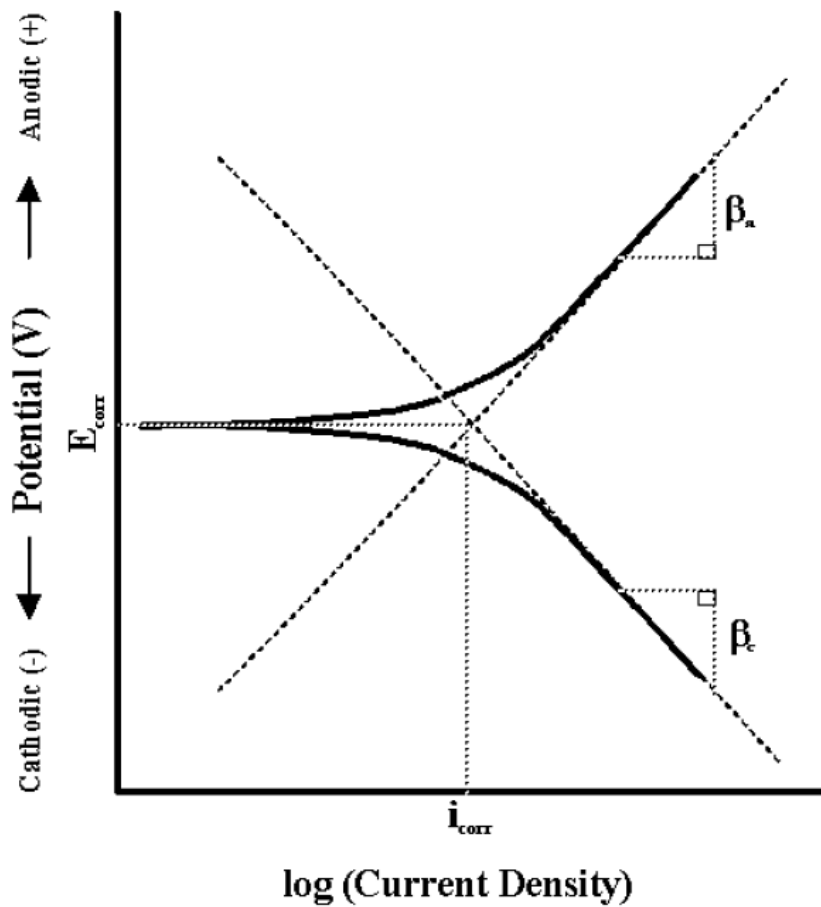


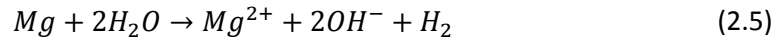
Figure 11: Tafel Plot showing the positive anodic Tafle slope β_a , negative cathodic Tafle slope β_c , and their linear extrapolations with their intersection indicating the OCP, and thus the i_{corr} and the E_{corr} positions [44].

2.4.2.2 Mg Hydrogen Evolution

The corrosion of Mg (equation (2.5)) results in the generation of molecular hydrogen gas products, in a process called hydrogen evolution [40]. This is problematic in biomedical applications as biodegradation of Mg alloys can result in the production of hydrogen gas cavities around the treatment area.

As noted in Witte [42] historical review of Mg implant clinical trials, generally these gas cavities were not considered painful and often subsided within days or weeks, with complete corrosion of implants

following shortly [45, 46]. The corrosion of the implants also did not appear to harm the surrounding tissues, showing no signs of irritation or inflammation [45]. Though excessive gas formation produced local swelling and significant pain, resulting in implants being prematurely removed [46]. However the cause of these critical failures were identified as resulting from the large potentials of electrically coupling Mg with Fe, and were not repeated [46].



As can be inferred from equation (2.5), the severity and quantity of H₂ gas generation via hydrogen evolution is dependent on the corrosion of the Mg. Thus the effects of hydrogen evolution can be greatly mediated by slowing the rate at which H₂ gas is generated via lowering the corrosion rate of Mg. Common methods employed to improve and inhibit Mg corrosion include the use of high-purity Mg alloys, alloying to promote the formation of protective passive films, and alloying to promote the formation of amorphous structures.

In devolving high corrosion resistance Mg alloys, Wang, et al. [39] have found amorphous and semi-crystalline Mg₆₇Zn₂₈Ca₅ alloy are able to quickly form a protective passive film to limit their corrosion rate and hydrogen evolution. Initially these alloys produce a moderate amount of H₂ gas, but the rate quickly drops off and results in a very small amount of total gas being release throughout the corrosion process [39]. In contrast, the fully crystalline alloy initially sees its H₂ gas release rate increase over time, before eventually reducing and stabling at a low level [39]. This occurs because initially it is difficult for the crystalline alloy to form the passive film, resulting in a high average rate and large total volume of gas release [39]. The release of large total amounts of hydrogen gas is closely linked to great amounts of specimen weight loss, meaning these crystalline alloys loss far more bulk material to the corrosion process than the amorphous ones, and hence would have shorter service lives [39].

Zberg, et al. [40] has also been particularly successful at reducing hydrogen evolution with amorphous Mg_{60+x}Zn_{35-x}Ca₅ alloys, showing the passive films generated by Zn can eliminate hydrogen evolution almost completely. From these studies, Zberg, et al. [40] showed Zn poor alloys produce significant hydrogen, while alloys with Zn contents greater than 28at% produced almost none. Additionally Zberg, et al. [40] conditioned animal trials on pigs of their alloys via implanting Mg disk of amorphous Mg₆₀Zn₃₅Ca₅ and crystalline Mg alloy (WZ21) within the abdominal walls for a period of three months. The wound-healing process was characterised as typical for both alloys with no inflammatory reactions observed for either [40]. However, examinations at the one and three month mark showed only hydrogen generation at the site of the crystalline alloy implants [40].

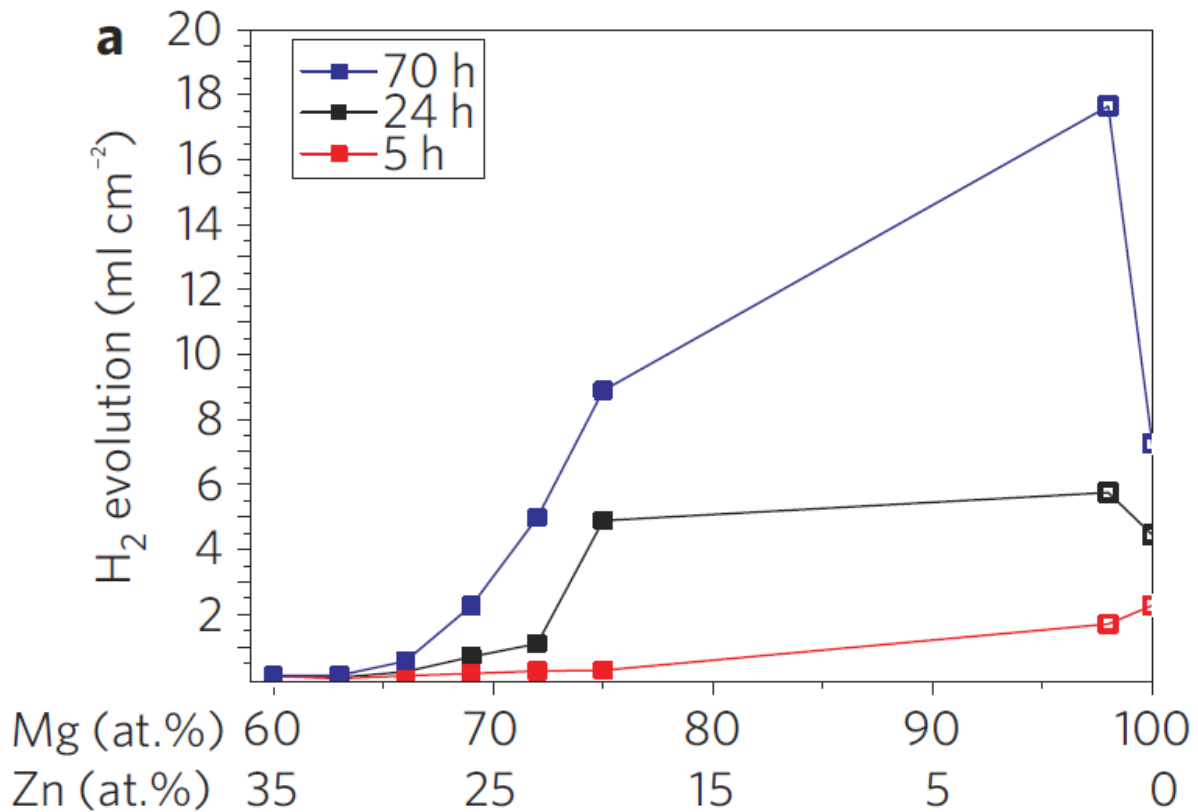


Figure 12: Plot of hydrogen evolution generated by $Mg_{60+x}Zn_{35-x}Ca_5$ alloys. Note the hydrogen evolution drops off significantly for Zn concentration $>28\text{at}\%$. (Filled points are amorphous, open crystalline). Reproduced from [40].

As Witte [42] has shown in his review magnesium was showing promise as a bio-reabsorbable material in the early 1900s before the trend switch to bio-inert materials like Ti.

Challenges with bio-reabsorbable metals, need to;

- Reduce the level of ion toxicity;
- Reduce the amount of hydrogen gas; and
- Control the loss of mechanical strength over time.

2.4.2.3 Pitting Corrosion

Generally pitting is associated with the breakdown of passive films, such as in stainless steels [41, 43, 47]. Pitting is associated with quenched in free volume surface defects in BMG [39].

Pitting corrosion is associated with the breakdown of the passive film (Reread page 41 of Jones fundamentals) [41, 43, 47]. This can be due to the presents of Cl^- ions [41].

BMG suffer from pitting corrosion because of quenched in free volume defects [39] (many more papers. Check later). Pitting increases with level of amorphousness [34].

Amorphous Mg allows for higher alloy continents and a homogeneous single-phase structure. These help improve corrosion characteristics.

Amorphous metal has high corrosion resistance due to

Chemical homogeneity

Monolithic structure

Lack of grain boundaries

Mg and Ca corrode in preference to Zn, leaving behind a Zn rich surface which promotes a passive layer [39].

Pitting occur on anodic end of the Tafel Plots [34].

2.4.3 Anti-biotic Scaffolds

3 METHODS

3.1 TARGET MANUFACTURE

The thin film metallic glasses (TFMGs) and ultrastable glasses (SMGs) are deposited onto various substrates via physical vapour deposition (PVD) processes.

3.1.1 Induction Furnace

The production of thin films via PVD processes first requires the manufacture of targets from pure base elements. This is accomplished via induction furnace and shaping operations.

3.1.1.1 Charges Preparation

The pure alloy constituent elements of Mg (99.85 wt%), Zn (99.995 wt%), and Ca (99.8 wt%) are polished and filed to removal surface contamination and oxides. The quantities of elements required are then checked via a developed MS Excel tool which calculates constituent element weights, checks alloy composition, and provides a form for notes on the induction casting process (i.e. heating cycles, observations, possible future refinements, etc.).

The screenshot shows an MS Excel spreadsheet titled 'MgZnCa - Props and Calcs - 2014 - Beta - Excel'. The spreadsheet is organized into several sections for calculating charge weights and alloy composition for Mg₆₅Zn₃₀Ca₅.

Charge Number 03 - 20 October 2014

At% to Wt% Charge Weight

	at%	at% * AW	wt%	Mass [g]	Charge [oz]
Mg ₆₅ Zn ₃₀ Ca ₅					
Mg	65.00%	15.79825	42.22%	47.686	27.437
Zn	30.00%	19.6146	52.42%	59.205	8.292
Ca	5.00%	2.0039	5.36%	6.049	3.902
Total	100.00%	37.41675	100.00%	112.94	39.632

Oxidised Weight Check (Wt% to At%)

	Mass [g]	wt%	wt11% * AW2/A W3	at%
Mg ₆₅ Zn ₃₀ Ca ₅				
Mg	48.035	42.57%	1110.15	65.13%
Zn	59.266	52.27%	509.1749	29.87%
Ca	6.080	5.36%	85.21521	5.00%
Total	113.381	100.00%	1704.54	100.00%

Charge At% & Elements Properties

Alloy Constituent	Element	Atomic Percent [%]	Atomic Number	Atomic Weight [amu]	Density [g/cm ³]	Melt Temp [°C]	Cry Struc [°C]	Atomic Radius [nm]	Ionic Radius [nm]	Most Common Valence
1	Mg	65.00%	12	24.305	1.738	650	HCP	0.136	0.072 2+	
2	Zn	30.00%	30	65.382	7.14	420	HCP	0.133	0.074 2+	
3	Ca	5.00%	20	40.078	1.55	842	FCC	0.149	0.095 2+	

Oxidised Weight of Pieces

	Mg	Zn	Ca
Pieces	Mass [g]	Pieces	Mass [g]
1	5.294	1	45.801
2	6.611	2	25.852
3	8.218	3	30.482
4	8.422	4	28.784
5	8.501	5	0
6	8.774	6	0
7	9.13	7	0
8	9.317	8	0
9	10.989	9	0
10	0	10	0

Cleaned Weight Check (Wt% to At%)

	Mass [g]	wt%	wt11% * AW2/A W3	at%
Mg ₆₅ Zn ₃₀ Ca ₅				
Mg	47.687	42.22%	1106.303	64.99%
Zn	59.184	52.40%	510.4062	29.98%
Ca	6.080	5.38%	85.53962	5.03%
Total	112.951	100.00%	1702.249	100.00%

Melting & Casting Cycle

Process	Temp [°C]	Notes
Heat 1	700	Alloy Tm about 400C
Cool 1	385	
Heat 2	650	
Cool 2	385	
Heat 3	650	
Cool 3	510	Casting Temp
Heat 4		
Cool 4		
Heat 5		
Cool 5		

Oxidised Pieces to be Casted

	Mg	Zn	Ca
Pieces	Mass [g]	Pieces	Mass [g]
1	5.294	3	30.482
2	6.611	4	28.784
3	8.218	0	0
4	8.422	0	0
5	8.501	0	0

Cleaned Weight of Pieces to be Casted

	Mg	Ox	Clean	%
Pieces	Mass [g]	Mass [g]	Mass [g]	Loss
1	5.294	5.282	0.23%	
2	6.611	6.59	0.32%	
3	8.218	8.179	0.47%	
4	8.422	8.385	0.44%	
5	8.501	8.485	0.19%	

Ca Ox Clean %

	Pieces	Mass [g]	Mass [g]	Loss
1	6.08	6.08	0.00%	
2	0	0	0	
3	0	0	0	
4	0	0	0	
5	0	0	0	

Figure 13: Screenshot of the MS Excel tool developed for calculating charge weights, checking alloy composition, and taking notes for improvements in future charges.

3.1.1.2 Induction Casting of Alloys

Thin 3mm plates of Mg₆₅Zn₃₀Ca₅ alloy are produced via melting the constituent elements in an induction furnace, under an inert Ar atmosphere, followed by gravity casting. The pure elements of Mg (99.85 wt%), Zn (99.995 wt%), and Ca (99.8 wt%) are introduced into the melt. Alloy homogeneity is ensured via following a multiple heating/cooling cycle between the alloy's solidus and liquidus states. The Mg₆₅Zn₃₀Ca₅ alloy cycle is; initial melting of all constituent elements together at 700°C, solidify at 385°C, remelt at 650°C, resolidify at 385°C, and remelt at 650°C. The melt is then cooled to a casting temperature of 510°C and gravity cast into a naturally cooled copper plate mould producing thin plate of the alloy.

3.1.2 Shaping of Targets

After casting the riser is cut off, and a target extracted from the amorphous plate via a slightly oversized diamond bit drill press. The amorphous target is then shaped into a nominally 1in (25.2 – 25.4mm) diameter disk via removal of excess pieces and finishing operations. The targets are then gradually polished on both sides to at least a P1200 grit, before they are suitable for use in the sputtering gun.

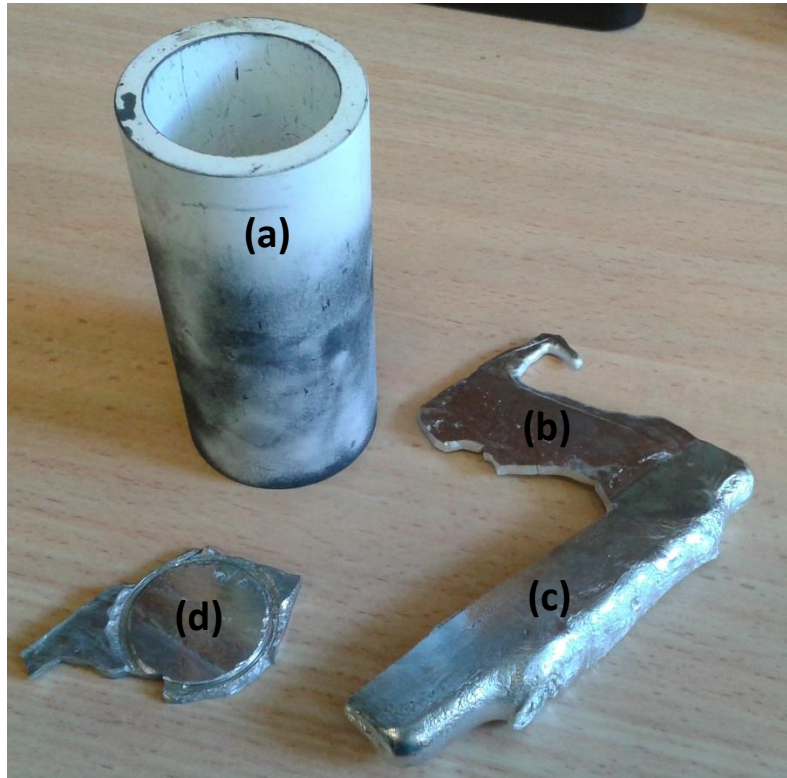


Figure 14: (a) Crucible for induction furnace melting of alloys, (b) cracked amorphous plate, (c) riser cut free from main casting, and (d) drilled and partly shaped target.

3.2 PVD VIA MAGNETRON SPUTTERING

3.2.1 Sputtering of TFMGs and SMGs

Each target is expected to be able to deposit approximately 10 – 15 μ m of total film thickness onto a substrate, which is about an hour of deposition at rate of 3.3nm/s. After full deposition the targets are no longer usable and should be disposed.

3.2.2 Sputtering Methods and Initial Parameters

Once placed in the sputtering gun the targets are prepared for deposition via a pre-sputter to remove contamination and oxides from their surface. The TFMGs are deposited onto room temperature substrates, and SMGs onto elevated temperature substrates. The elevated temperatures are achieved and controlled via hot plate and thermocouple.

The initial TFMG sputtering parameters will be based on Liu, et al. [21] work on $Zr_{55}Cu_{30}Ni_5Al_{10}$ film refinement, and the SMG parameters will be based on Yu, et al. [28] and Aji, et al. [3] work on $Zr_{65}Cu_{27.5}Al_{7.5}$ and $Zr_{55}Cu_{30}Ni_5Al_{10}$ SMG films respectively. These parameters will be refined via appropriate step sizes as required to suit the examined MgZnCa biocompatible systems.

Nominal Sputtering Parameters:	TFMG	SMG
Base Chamber Pressure:	$3 \times 10^{-4} - 10^{-2}$ Pa	$5 \times 10^{-5} - 10^{-4}$ Pa
Deposition Ar Pressure:	0.3 – 3.0 Pa	$5 \times 10^{-2} - 0.3$ Pa
Deposition Power Range:	30 – 50 W	30 – 50 W
Max Deposition Rate: (To be determined via TEM)	3.3 nm s^{-1}	1.4 nm s^{-1}
Substrate Deposition Temperature:	Room Temperature	$0.7 - 0.8 T_g$

3.3 EXAMINED SUBSTRATES

The films will be deposited onto three different substrates for examination; water soluble substrate, BMG substrates, and PCL scaffold substrates.

3.3.1 Water Soluble Substrate

Depositing films onto water soluble substrates allows the films be physically separated from a substrate and examined without their influence. A possible candidate substrates is NaCl wafer which dissolve quickly with the application of water, allowing for the physical separation of the films. These substrates can be purchased.

3.3.2 BMG Substrate

Depositing films onto BMG substrates of similar composition allows for property modification effects of the films to be examined. Knowing the properties of the BMG substrates and the applied films independently will allow the extent of the property modification to be fully evaluated, and should allow for modelling. These substrates can be produced via the same methods used to produce targets.

3.3.3 Polycaprolactone (PCL) Scaffolds

Depositing films onto Polycaprolactone (PCL) scaffolds substrates will allow for examination of the films' effects and degradation performance. Ideally this will lead to the slow, controlled release of infused with antimicrobial, antibiotic, or analgesics packages.

3.4 FILM CHARACTERISATION

The properties of the TFMGs and SMGs will be investigated via characterising the films after application to the different substrates; allowing standalone films as well as their substrate property modification effects to be investigated.

3.4.1 Physical and Chemical Properties

The physical and chemical properties of the films will be characterised via a range of techniques; XRD, DSC, FIB-SEM, EPMA, ICP, STEM, ABED, etc.

3.4.2 Biocompatibility and Bioabsorption

The biocompatibility and bioabsorption of the TFMGs will be characterised via cytotoxicity testing, PDP scans, etc.

3.4.3 Quality of Deposition

The quality of the TFMG deposition will be ascertained via investigation of the surface finish, coating adhesion, bonding, etc.

4 PRELIMINARY RESULTS

4.1 EXPERIMENTAL RESULTS

4.1.1 Casting Challenges and Observations

When casting the target plates it was found slow melt pouring resulted in a poor mould fill while quicker pour experienced greater fills. The thin plate and relatively large mould riser creates a notable cooling difference between the two sections within the casting. It is believe this temperature gradient encourages the formation of cracks which often make the casting unusable. Additionally, the casting often display porosity within the plate, which may result in increased brittleness of the material.

4.1.2 DSC Scans

Isochoric DSC scans are performed as a simple check for amorphous alloy structure via looking for evidence of the distinct exothermal T_g and T_x recrystallization peaks, and the endothermal T_m and T_l toughs. Scans are performed at heating rate of 20K/min in sealed alumina crucibles under a protective Ar atmosphere.

4.1.3 Target Composition

Ideal $\text{Mg}_{65}\text{Zn}_{30}\text{Ca}_5$ targets should be completely amorphous as this should make them more resistance to corrosion before use, and provide a more homogenous distribution of constructional elements within the targets. The initial DSC scans of the targets produced thus far do not display clear exothermal peaks, indicating they are not fully amorphous. However it is possible the targets are semi-crystalline, especially given how subtle exothermal peaks can be in MgZnCa systems [48].

It is expected XRD analysis may be able to provide more detail into the structure of the target plates as this technique has proven effective in differentiating between amorphous, semi-crystalline, and crystalline MgZnCa alloy [34, 39], although it can still be difficult [49]. Fully amorphous MgZnCa should display wide halo peaks around 38° and 66° (2 theta) and no additional sharp peaks, while semi-crystalline alloy would start to displace additional peaks [39, 48, 50, 51].

Alloys of similar composition, like $\text{Mg}_{70}\text{Zn}_{25}\text{Ca}_5$, have a low GFA with a t_{max} of only about 3mm [49, 52]. This coupled with the casting riser's (Figure 14 (c)) ability to hold heat and thus extend the solidification time provides evidence that some amount of crystallization should be expected within the plate casting.

The work of Schlüter, et al. [34], Zhou, et al. [49], and Wang, et al. [39] on $\text{Mg}_{60}\text{Zn}_{35}\text{Ca}_5$, $\text{Mg}_{70}\text{Zn}_{25}\text{Ca}_5$, and $\text{Mg}_{67}\text{Zn}_{28}\text{Ca}_5$ respectively shows, semi-crystalline structures display both lower corrosion current density and more noble corrosion potential in comparison to fully crystalline alloy, and similar values to amorphous alloy. Hence semi-crystalline targets are expected to be relatively stable from crystalline galvanic/intergranular corrosion between the alloy constituents.

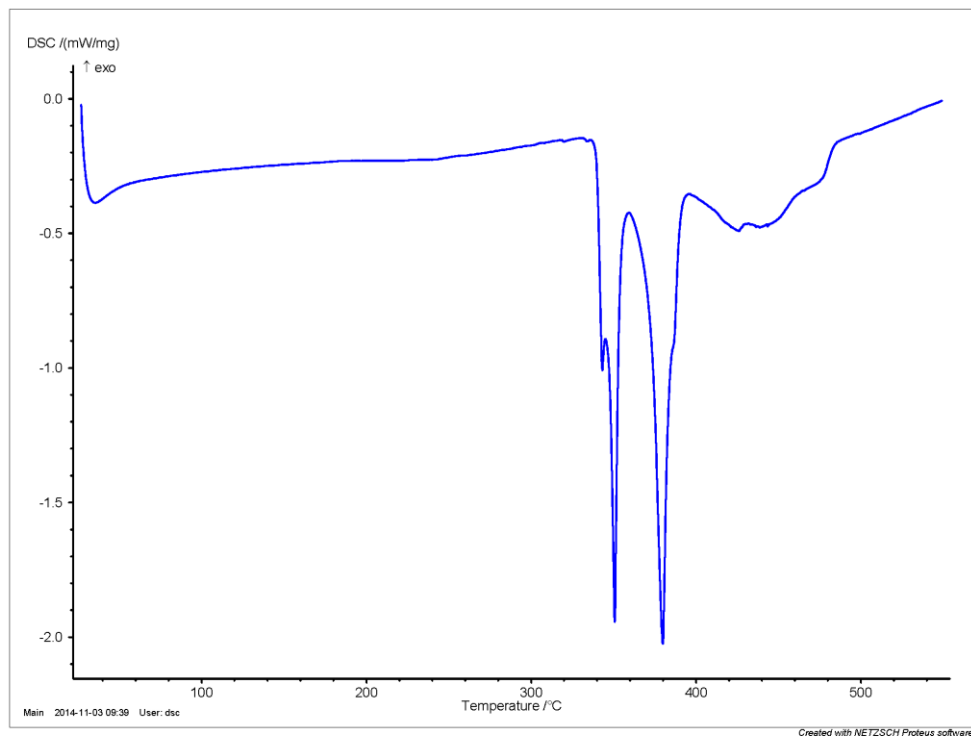


Figure 15: DSC trace of the $Mg_{65}Zn_{30}Ca_5$ target plate casting. The trace shows clear endothermic troughs indicating T_m and T_l , but no clear exothermal peaks which would indicate T_g and T_x . This data suggest the casting is primary crystalline.

However Zhou, et al. [49] has shown that despite this amorphous alloy has increased cathodic reaction kinetics and decreased anodic reaction when compared to CP Mg, suggesting the corrosion rate of amorphous and semi-crystalline alloys is not significantly different from pure Mg.

5 REFERENCES

- [1] A. L. Greer, Y. Q. Cheng, and E. Ma, "Shear bands in metallic glasses," *Materials Science and Engineering: R: Reports*, vol. 74, pp. 71-132, 4// 2013.
- [2] M. Ediger, C. Angell, and S. R. Nagel, "Supercooled liquids and glasses," *The journal of physical chemistry*, vol. 100, pp. 13200-13212, 1996.
- [3] D. P. Aji, A. Hirata, F. Zhu, L. Pan, K. M. Reddy, S. Song, *et al.*, "Ultrastrong and Ultrastable Metallic Glass," *arXiv preprint arXiv:1306.1575*, 2013.
- [4] W. Klement, R. Willens, and P. Duwez, "Non-crystalline structure in solidified gold–silicon alloys," 1960.
- [5] A. Inoue, "Stabilization of metallic supercooled liquid and bulk amorphous alloys," *Acta Materialia*, vol. 48, pp. 279-306, 1/1/ 2000.
- [6] M. M. Trexler and N. N. Thadhani, "Mechanical properties of bulk metallic glasses," *Progress in Materials Science*, vol. 55, pp. 759-839, 11// 2010.
- [7] J. Schroers, "Processing of Bulk Metallic Glass," *Advanced Materials*, vol. 22, pp. 1566-1597, 2010.
- [8] J. P. Chu, J. E. Greene, J. S. C. Jang, J. C. Huang, Y.-L. Shen, P. K. Liaw, *et al.*, "Bendable bulk metallic glass: Effects of a thin, adhesive, strong, and ductile coating," *Acta Materialia*, vol. 60, pp. 3226-3238, 4// 2012.
- [9] F. X. Liu, F. Q. Yang, Y. F. Gao, W. H. Jiang, Y. F. Guan, P. D. Rack, *et al.*, "Micro-scratch study of a magnetron-sputtered Zr-based metallic-glass film," *Surface and Coatings Technology*, vol. 203, pp. 3480-3484, 8/15/ 2009.
- [10] B. Prakash, "Abrasive wear behaviour of Fe, Co and Ni based metallic glasses," *Wear*, vol. 258, pp. 217-224, 1// 2005.
- [11] C. L. Chiang, J. P. Chu, F. X. Liu, P. K. Liaw, and R. A. Buchanan, "A 200nm thick glass-forming metallic film for fatigue-property enhancements," *Applied Physics Letters*, vol. 88, pp. -, 2006.
- [12] J. P. Chu, C. M. Lee, R. T. Huang, and P. K. Liaw, "Zr-based glass-forming film for fatigue-property improvements of 316L stainless steel: Annealing effects," *Surface and Coatings Technology*, vol. 205, pp. 4030-4034, 5/15/ 2011.
- [13] C. W. Chu, J. S. C. Jang, S. M. Chiu, and J. P. Chu, "Study of the characteristics and corrosion behavior for the Zr-based metallic glass thin film fabricated by pulse magnetron sputtering process," *Thin Solid Films*, vol. 517, pp. 4930-4933, 7/1/ 2009.
- [14] P. H. Tsai, Y. Z. Lin, J. B. Li, S. R. Jian, J. S. C. Jang, C. Li, *et al.*, "Sharpness improvement of surgical blade by means of ZrCuAlAgSi metallic glass and metallic glass thin film coating," *Intermetallics*, vol. 31, pp. 127-131, 12// 2012.
- [15] J. P. Chu, J. S. C. Jang, J. C. Huang, H. S. Chou, Y. Yang, J. C. Ye, *et al.*, "Thin film metallic glasses: Unique properties and potential applications," *Thin Solid Films*, vol. 520, pp. 5097-5122, 6/1/ 2012.
- [16] H. U. Krebs and O. Bremert, "Pulsed laser deposition of thin metallic alloys," *Applied Physics Letters*, vol. 62, pp. 2341-2343, 1993.
- [17] D. Dijkkamp, T. Venkatesan, X. Wu, S. Shaheen, N. Jisrawi, Y. Min-Lee, *et al.*, "Preparation of Y-Ba-Cu oxide superconductor thin films using pulsed laser evaporation from high T_c bulk material," *Applied Physics Letters*, vol. 51, pp. 619-621, 1987.
- [18] J. Heitz, X. Wang, P. Schwab, D. Bäuerle, and L. Schultz, "KrF laser-induced ablation and patterning of Y–Ba–Cu–O films," *Journal of Applied Physics*, vol. 68, pp. 2512-2514, 1990.
- [19] J. D. Cao, "Processing and properties of biocompatible metallic glasses," M. Ferry and K. Laws, Eds., ed: Thesis (Ph.D) - University of New South Wales - Australia, 2013.
- [20] T. E. Brown, T. L. Brown, H. E. H. LeMay, B. E. Bursten, C. Murphy, and P. Woodward, *Chemistry: The Central Science*: Pearson Education, 2014.

- [21] Y. H. Liu, T. Fujita, A. Hirata, S. Li, H. W. Liu, W. Zhang, *et al.*, "Deposition of multicomponent metallic glass films by single-target magnetron sputtering," *Intermetallics*, vol. 21, pp. 105-114, 2// 2012.
- [22] K. Kondoh, K. Kawabata, T. Serikawa, and H. Kimura, "Structural Characteristics and Crystallization of Metallic Glass Sputtered Films by Using Zr System Target," *Advances in Materials Science and Engineering*, vol. 2008, 2008.
- [23] Y. P. Deng, Y. F. Guan, J. D. Fowlkes, S. Q. Wen, F. X. Liu, G. M. Pharr, *et al.*, "A combinatorial thin film sputtering approach for synthesizing and characterizing ternary ZrCuAl metallic glasses," *Intermetallics*, vol. 15, pp. 1208-1216, 9// 2007.
- [24] J. Qin, X. Yong, Z. Xin-Yu, L. Gong, L. Li-Xin, X. Zhe, *et al.*, "Zr-Cu amorphous films prepared by magnetron co-sputtering deposition of pure Zr and Cu," *Chinese Physics Letters*, vol. 26, p. 086109, 2009.
- [25] M. Apreutesei, P. Steyer, L. Joly-Pottuz, A. Billard, J. Qiao, S. Cardinal, *et al.*, "Microstructural, thermal and mechanical behavior of co-sputtered binary Zr–Cu thin film metallic glasses," *Thin Solid Films*, vol. 561, pp. 53-59, 6/30/ 2014.
- [26] S. F. Swallen, K. L. Kearns, M. K. Mapes, Y. S. Kim, R. J. McMahon, M. D. Ediger, *et al.*, "Organic glasses with exceptional thermodynamic and kinetic stability," *Science*, vol. 315, pp. 353-356, 2007.
- [27] K. Dawson, L. Zhu, L. A. Kopff, R. J. McMahon, L. Yu, and M. Ediger, "Highly stable vapor-deposited glasses of four tris-naphthylbenzene isomers," *The Journal of Physical Chemistry Letters*, vol. 2, pp. 2683-2687, 2011.
- [28] H.-B. Yu, Y. Luo, and K. Samwer, "Ultrastable Metallic Glass," *Advanced Materials*, vol. 25, pp. 5904-5908, 2013.
- [29] J. Q. Wang, N. Chen, P. Liu, Z. Wang, D. V. Louzguine-Luzgin, M. W. Chen, *et al.*, "The ultrastable kinetic behavior of an Au-based nanoglass," *Acta Materialia*, vol. 79, pp. 30-36, 10/15/ 2014.
- [30] K. J. Dawson, L. Zhu, L. Yu, and M. Ediger, "Anisotropic structure and transformation kinetics of vapor-deposited indomethacin glasses," *The Journal of Physical Chemistry B*, vol. 115, pp. 455-463, 2010.
- [31] K. L. Kearns, S. F. Swallen, M. Ediger, T. Wu, Y. Sun, and L. Yu, "Hiking down the energy landscape: Progress toward the Kauzmann temperature via vapor deposition," *The Journal of Physical Chemistry B*, vol. 112, pp. 4934-4942, 2008.
- [32] Y. Guo, A. Morozov, D. Schneider, J. W. Chung, C. Zhang, M. Waldmann, *et al.*, "Ultrastable nanostructured polymer glasses," *Nature materials*, vol. 11, pp. 337-343, 2012.
- [33] J. E. Shelby, *Introduction to Glass Science and Technology*: Royal Society of Chemistry, 2005.
- [34] K. Schlüter, C. Zamponi, N. Hort, K. U. Kainer, and E. Quandt, "Polycrystalline and amorphous MgZnCa thin films," *Corrosion Science*, vol. 63, pp. 234-238, 10// 2012.
- [35] S. J. Bull and A. M. Jones, "Multilayer coatings for improved performance," *Surface and Coatings Technology*, vol. 78, pp. 173-184, 1// 1996.
- [36] P. J. Burnett and D. S. Rickerby, "The relationship between hardness and scratch adhesion," *Thin Solid Films*, vol. 154, pp. 403-416, 11/12/ 1987.
- [37] P. J. Burnett and D. S. Rickerby, "The scratch adhesion test: An elastic-plastic indentation analysis," *Thin Solid Films*, vol. 157, pp. 233-254, 2/29/ 1988.
- [38] C. T. Pan, T. T. Wu, C. F. Liu, C. Y. Su, W. J. Wang, and J. C. Huang, "Study of scratching Mg-based BMG using nanoindenter with Berkovich probe," *Materials Science and Engineering: A*, vol. 527, pp. 2342-2349, 4/15/ 2010.
- [39] Y. Wang, M. J. Tan, J. Pang, Z. Wang, and A. W. E. Jarfors, "In vitro corrosion behaviors of Mg₆₇Zn₂₈Ca₅ alloy: From amorphous to crystalline," *Materials Chemistry and Physics*, vol. 134, pp. 1079-1087, 6/15/ 2012.
- [40] B. Zberg, P. J. Uggowitzer, and J. F. Löffler, "MgZnCa glasses without clinically observable hydrogen evolution for biodegradable implants," *Nature Materials*, vol. 8, pp. 887-891, 2009.

- [41] Y. F. Zheng, X. N. Gu, and F. Witte, "Biodegradable metals," *Materials Science and Engineering: R: Reports*, vol. 77, pp. 1-34, 3// 2014.
- [42] F. Witte, "The history of biodegradable magnesium implants: A review," *Acta Biomaterialia*, vol. 6, pp. 1680-1692, 5// 2010.
- [43] D. A. Jones, *Principles and prevention of corrosion*: Macmillan, 1992.
- [44] D. G. Enos and L. Scribner, "The potentiodynamic polarization scan," *Center for Electrochemical Science & Engineering*, 1997.
- [45] J. Verbrugge, "La tolérance du tissu osseux vis-à-vis du magnésium métallique," *Presse méd*, vol. 55, pp. 1112-1114, 1933.
- [46] A. Lambotte, "L'utilisation du magnésium comme matériel perdu dans l'osteosynthèse," *Bull Mem Soc Nat Chir*, vol. 28, pp. 1325-1334, 1932.
- [47] P. A. Schweitzer, *Fundamentals of corrosion: mechanisms, causes, and preventative methods*: CRC Press, 2009.
- [48] X. Gu, Y. Zheng, S. Zhong, T. Xi, J. Wang, and W. Wang, "Corrosion of, and cellular responses to Mg–Zn–Ca bulk metallic glasses," *Biomaterials*, vol. 31, pp. 1093-1103, 2// 2010.
- [49] X. Zhou, K. D. Ralston, K. J. Laws, J. D. Cao, R. K. Gupta, M. Ferry, *et al.*, "Effect of the Degree of Crystallinity on the Electrochemical Behavior of Mg₆₅Cu₂₅Y₁₀ and Mg₇₀Zn₂₅Ca₅ Bulk Metallic Glasses," *Corrosion*, vol. 69, pp. 781-792, 2013/08/01 2013.
- [50] J. D. Cao, P. Martens, K. J. Laws, P. Boughton, and M. Ferry, "Quantitative in vitro assessment of Mg₆₅Zn₃₀Ca₅ degradation and its effect on cell viability," *Journal of Biomedical Materials Research Part B: Applied Biomaterials*, vol. 101B, pp. 43-49, 2013.
- [51] J. D. Cao, K. J. Laws, N. Birbilis, and M. Ferry, "Potentiodynamic polarisation study of bulk metallic glasses based on the Mg–Zn–Ca ternary system," *Corrosion Engineering, Science and Technology*, vol. 47, pp. 329-334, 2012.
- [52] X. Gu, G. J. Shiflet, F. Q. Guo, and S. J. Poon, "Mg–Ca–Zn Bulk Metallic Glasses with High Strength and Significant Ductility," *Journal of Materials Research*, vol. 20, pp. 1935-1938, 2005.

6 APPENDICES

6.1 GLOSSARY

ABED	–	Angstrom Beam Electron Diffraction
BMG	–	Bulk Metallic Glass
C_p	–	Specific Heat Capacity (J / gK)
CVD	–	Chemical Vapour Deposition
DC	–	Direct Current (I)
DSC	–	Differential Scanning Calorimetry
E	–	Young's Modulus (GPa)
E_A	–	Applied Potential (V)
E_{OCP}	–	Open Circuit Potential (V)
E_{corr}	–	Corrosion Potential (V)
FDA	–	Food and Drug Administration
GFA	–	Glass Forming Ability
H	–	Enthalpy (J)
h	–	Specific Enthalpy (J / g)
i	–	Current Density (A/cm ²)
i_0	–	Exchange Current Density (A/cm ²)
i_{corr}	–	Corrosion Current Density (A/cm ²)
m	–	Fragility
MG	–	Metallic Glass
MRO	–	Medium Range Order
PCL	–	Polycaprolactone
PDP	–	Potentiodynamic Polarisation
PLD	–	Pulse Laser Deposition
PVD	–	Physical Vapour Deposition
R_c	–	Critical Cooling Rate (K / s)
S	–	Entropy (J / K)
s	–	Specific Entropy (J / gK)

SCL	–	Super Cooled Liquid
SCLR	–	Super Cooled Liquid Region
SMG	–	Ultrastable Metallic Glass
T	–	Temperature (K)
T_f	–	Fictive Temperature (K)
TFMG	–	Thin Film Metallic Glass
T_g	–	Glass Transition Temperature (K)
TGA	–	Therapeutic Goods Administration
T_g/T_m	–	Reduced Glass Transition Temperature
T_k	–	Kauzmann Temperature (K)
T_l	–	Liquidus Temperature (K)
T_m	–	Melting Temperature (K)
T_{onset}	–	Onset Temperature (K)
TPF	–	Thermoplastic Forming
T_{sub}	–	Substrate Temperature (K)
t_{max}	–	Maximum Sample Thickness (mm)
T_x	–	Crystallisation Temperature (K)
STEM	–	Scan Transmission Electron Microscopy
UHV	–	Ultrahigh Vacuum
UNSW	–	University of New South Wales
USG	–	Ultrastable Glass
V	–	Volume (m^3)
v	–	Specific Volume (m^3 / kg)
VD	–	Vapour Deposition
β	–	Tafel Slope
ΔT	–	Super Cooled Liquid Region (K)
δT_g	–	Enhanced Glass Transition Temperature (K)
η	–	Viscosity ($Pa s$)
η	–	Overpotential (V)
θ_k	–	Proportion along the Energy Landscape